

Lead-substituted barium hexaferrite for tunable terahertz optoelectronics

Liudmila Alyabyeva (✉ aliabeva.ln@mipt.ru)

Moscow Institute of Physics and Technology (National Research University) <https://orcid.org/0000-0001-8238-4674>

Anatoly Prokhorov

A.M. Prokhorov General Physics Institute, Russian Academy of Sciences

Denis Vinnik

South Ural State University

Vladimir Anzin

Moscow Institute of Physics and Technology (National Research University)

Asmaa Ahmed

Moscow Institute of Physics and Technology (National Research University)

Aleksey Mikheykin

Southern Federal University

Petr Bednyakov

Institute of Physics of the Czech Academy of Science

Christelle Kadlec

Institute of Physics of the Czech Academy of Sciences <https://orcid.org/0000-0003-2820-4462>

Filip Kadlec

Institute of Physics, The Czech Academy of Sciences

Esther de Prado

Institute of Physics of the Czech Academy of Science

Jan Prokleška

Charles University, Faculty of Mathematics and Physics

Petr Proschek

Charles University

Stanislav Kamba

Institute of Physics of the Czech Academy of Sciences <https://orcid.org/0000-0003-4699-869X>

Artem Pronin

Physikalisches Institut, Universität Stuttgart

Martin Dressel

Physikalisches Institut, Universität Stuttgart

Veniamin Abalmasov

Institute of Automation and Electrometry SB RAS

Vyacheslav Dremov

Moscow Institute of Physics and Technology

Sebastian Schmid

University of Augsburg

Maxim Savinov

Institute of Physics, Academy of Science of Czech Republic

Peter Lunkenheimer

University of Augsburg <https://orcid.org/0000-0002-4525-1394>

Boris Gorshunov

Moscow Institute of Physics and Technology (National Research University)

Article

Keywords: Next-generation Communication Systems, Targeted Tuning, Broad-band Dielectric Response, Electronic Devices

Posted Date: May 3rd, 2021

DOI: <https://doi.org/10.21203/rs.3.rs-492476/v1>

License:   This work is licensed under a Creative Commons Attribution 4.0 International License.

[Read Full License](#)

Version of Record: A version of this preprint was published at NPG Asia Materials on September 17th, 2021. See the published version at <https://doi.org/10.1038/s41427-021-00331-x>.

Lead-substituted barium hexaferrite for tunable terahertz optoelectronics

Alyabyeva L.N.¹, Prokhorov A.S.^{1,2}, Vinnik D.A.³, Anzin V.B.^{1,2}, Ahmed A.G.^{1,4}, Mikheykin A.⁵, Bednyakov P.⁶, Kadlec C.⁶, Kadlec F.⁶, de Prado E.⁶, Prokleška J.⁷, Proschek P.⁷, Kamba S.⁶, Pronin A.V.⁸, Dressel M.^{1,8}, Abalmasov V.A.⁹, Dremov V.V.¹, Schmid S.¹⁰, Savinov M.⁶, Lunkenheimer P.¹⁰, Gorshunov B.P.¹

¹Laboratory of Terahertz Spectroscopy, Center for Photonics and 2D Materials, Moscow Institute of Physics and Technology (National Research University), Dolgoprudny, Russia

²Prokhorov General Physics Institute of the Russian Academy of Sciences, 119991, Moscow, Russia

³South Ural State University, 454080 Chelyabinsk, Russia

⁴Department of Physics, Faculty of Science, Sohag University, Sohag University St, Sohag, Egypt

⁵Southern Federal University, 344006, Rostov-on-Don, Russia

⁶Institute of Physics of the Czech Academy of Sciences, Praha 8, 18221, Czech Republic

⁷Faculty of Mathematics and Physics, Charles University, 12116 Prague 2, Czech Republic

⁸1. Physikalisches Institut, Universität Stuttgart, D-70550, Stuttgart, Germany

⁹Institute of Automation and Electrometry SB RAS, 630090 Novosibirsk, Russia

¹⁰Experimental Physics V, Center for Electronic Correlations and Magnetism, University of Augsburg, 86159 Augsburg, Germany

^aCorresponding author: aliabeva.ln@mipt.ru

Abstract

In recent years, due to their outstanding dielectric and magnetic properties, hexagonal ferrites (hexaferrites) have attracted considerable interest for developing electronic components of next-generation communication systems. The complex crystal structure of hexaferrites and critical dependences of their electric and magnetic properties on external factors, like magnetic or

electric fields, pressure or doping, open ample opportunities for targeted tuning of these properties when designing specific devices. To that end, we explored the electromagnetic properties of the Pb-substituted barium hexaferrite, $\text{Ba}_{1-x}\text{Pb}_x\text{Fe}_{12}\text{O}_{19}$, a compound featuring an extremely rich set of physical phenomena that are inherent in the dielectric and magnetic subsystems of the material and are expected to have significant effect on its electromagnetic response at radio and terahertz frequencies. We performed the first detailed measurements of the AC response of single-crystalline $\text{Ba}_{1-x}\text{Pb}_x\text{Fe}_{12}\text{O}_{19}$ in an extremely broad spectral range from 1 Hz to 240 THz down to temperatures as low as 5 K. We fully characterized numerous microscopic phenomena that determine the broad-band dielectric response of the compound, and we analyzed their nature. This includes temperature-activated radiofrequency relaxations that were attributed to the dynamic response of magnetic/dielectric domains. The terahertz response is dominated by a ferroelectric-like soft mode with an unusual temperature behavior that we explain by means of a microscopic model. Several narrower terahertz excitations are associated with electronic transitions between the fine-structure components of the Fe^{2+} ground state. Narrow resonances detected in the gigahertz region are presumably of magneto-electric origin. The obtained data on diverse but controllable electromagnetic properties of $\text{Ba}_{1-x}\text{Pb}_x\text{Fe}_{12}\text{O}_{19}$ compounds provides the researchers with information that makes the entire class of hexaferrites materials attractive for manufacturing electronic devices for the radiofrequency and terahertz ranges, such as absorbing coatings, anti-reflective coatings, absorbers, electromagnetic shields, antennas, phase shifters, filters, resonators, modulators, etc.

1. Introduction.

The terahertz (THz) frequency region has been the “dark horse” for the scientific community as far as technology and application is concerned. Although the theoretical predictions were rather exciting, the experimental potential did not allow to explore the proposed effects directly¹. This has changed, however, and the extensive search for materials in recent years begins to cover the

demands of the newly developed field of THz electronics. By now, the field of THz technologies is one of the most promising directions of the development of the electronics². The recently promoted 5G standard for broadband cellular networks operates at frequencies of tens of gigahertz. The upcoming 6G standard aims at even higher frequencies³, and the subsequent generations will inevitably move towards the THz region. The application of THz frequencies is not limited to the telecommunications, but it spans into radar systems, ultra-fast computer memories, non-destructive testing, safe bio-scanning, security imaging and many others^[4-6]. The crucial need of materials with desired properties for the particular applications becomes the bottleneck for the development of THz technology. Since it is in the terahertz region that the characteristic electronic, magnetic and mixed-type excitations are often found, the important scientific challenge that needs to be addressed involves the search for materials whose fundamental physical properties would most adequately meet the requirements of modern technological development.

In this respect, hexaferrites recently drew considerable interest due to their distinct dielectric, magnetic and mainly magnetoelectric properties (tunability of losses and dielectric constant, giant magnetoelasticity, multiferroicity, quantum paraelectricity)⁷⁻¹³ suitable for microwave and THz applications¹⁴⁻¹⁷. For example, ferrimagnetic BaFe₁₂O₁₉ with M-type hexaferrite crystal structure (denoted as BaM in the following) is the most widely commercially produced magnetic material with overall yearly market sales of billions of dollars¹⁸. Functional characteristics of substituted hexaferrites show an outstanding sensitivity to doping, making these materials the future candidates for novel devices of THz optoelectronics. Doped M-type hexaferrites exhibit superior magnetic characteristics, including the ferromagnetic resonance frequency located in the THz range, record values of the coercive force of up to 40 kOe¹⁹, and formation of a new type of Jahn-Teller sub-lattice²⁰. Doping BaM with lead is expected to systematically change its dielectric properties. In fact, the BaM is relatively transparent in the THz range²¹, whereas the lead ferrite PbFe₁₂O₁₉ effectively shields the THz radiation²². Despite

constituting a core material for the magnetic device market, hexaferrites are rather poorly studied from the dielectric standpoint. In other words, the practical development of this promising class of materials calls for thorough studies of their fundamental physical properties. In particular, this concerns fundamental processes that determine the electromagnetic properties of hexaferrites at THz frequencies. However, data on their electromagnetic responses, including that in the THz range, is lacking to date.

To fill up this gap, we report here on characterization of the electromagnetic properties in the Hz to THz frequency range of one of the most known representatives of the hexaferrites family, the lead-substituted barium hexaferrite $\text{Ba}_{1-x}\text{Pb}_x\text{Fe}_{12}\text{O}_{19}$ ($x=0.1, 0.2$). For the studies, we managed to synthesize a series of unique high-quality single crystals of the compounds. We found that their THz dielectric responses include strong soft excitations that can be easily tuned by temperature variation. The discovered THz resonance (“soft mode”) exhibits a highly unusual temperature behavior never detected in hexaferrites or other incipient ferroelectrics. We explain the non-classic temperature dynamics of this “soft mode” on a microscopic level. Moreover, in the Hz-MHz region, several temperature-activated relaxation processes were detected. In addition, we observed signs of an almost temperature-independent narrow resonance in the gigahertz region. Together with infrared (IR) lattice vibrations, the observed broadband electromagnetic response in the studied hexaferrites spans over 14 decades in frequency, and it involves processes of different natures; this enables us to draw a global picture of the microscopic mechanisms responsible for the observed phenomena. In this work we demonstrate that admixing Pb dramatically alters the THz response of the BaM. The possibility of effective targeted tuning of the functional characteristics of substituted hexaferrites by doping significantly extends the area of their applications in THz electronics.

2. Results and discussion

In the following, we first focus on a detailed consideration of the spectra and spectral features that we observed at different frequencies and at different temperatures, offer an interpretation of the phenomena that are at the origin of these features, and in the concluding section we consider our results in the context of the possibility of their practical use.

2.1. Broad-band electromagnetic spectrum of $\text{Ba}_{1-x}\text{Pb}_x\text{Fe}_{12}\text{O}_{19}$

For the $\text{Ba}_{1-x}\text{Pb}_x\text{Fe}_{12}\text{O}_{19}$, $x=0.2$ sample, the spectrum of complex dielectric permittivity in the range from 1 Hz to 30 THz (10^{-11} - 10^3 cm^{-1}) is shown in Fig. 1 (a,b). The phonon resonances (sharp peaks above 80 cm^{-1}) are nearly temperature independent down to $T = 10 \text{ K}$: all IR spectra practically coincide at frequencies above $\approx 100 \text{ cm}^{-1}$. The low-temperature drop in the intensity of the phonon peak at $\approx 90 \text{ cm}^{-1}$ is caused by softening of the THz absorption band as will be discussed below. For an extended picture of the IR phonon resonances for both compounds under study, see Supplemental Information, section SI2. The spectral response of the lattice vibrations observed in our compound is in line with the results obtained in other isostructural phases, such as the pure BaM²¹ and Pb-substituted $\text{Ba}_{0.3}\text{Pb}_{0.7}\text{Fe}_{12}\text{O}_{19}$ ²³. The resonances in the spectra were modeled by Lorentzian expressions for the complex permittivity

$$\varepsilon^*(\nu) = \varepsilon'(\nu) + i\varepsilon''(\nu) = \sum_j \frac{f_j}{\nu_j^2 - \nu^2 + i\nu\gamma_j} + \varepsilon_\infty, (1)$$

where $f_j = \Delta\varepsilon_j \nu_j^2$ is the oscillator strength of the j -th resonance, $\Delta\varepsilon_j$ is its dielectric strength, ν_j represents the resonance frequency, γ_j is the damping factor, and ε_∞ is the high-frequency dielectric constant. We used the high-frequency dispersion-free parts of reflectivity spectra (Fig. SI2-2) to determine the ε_∞ values: $\varepsilon_\infty = 7.06$ for $x=0.1$ and $\varepsilon_\infty = 6.92$ for $x=0.2$.

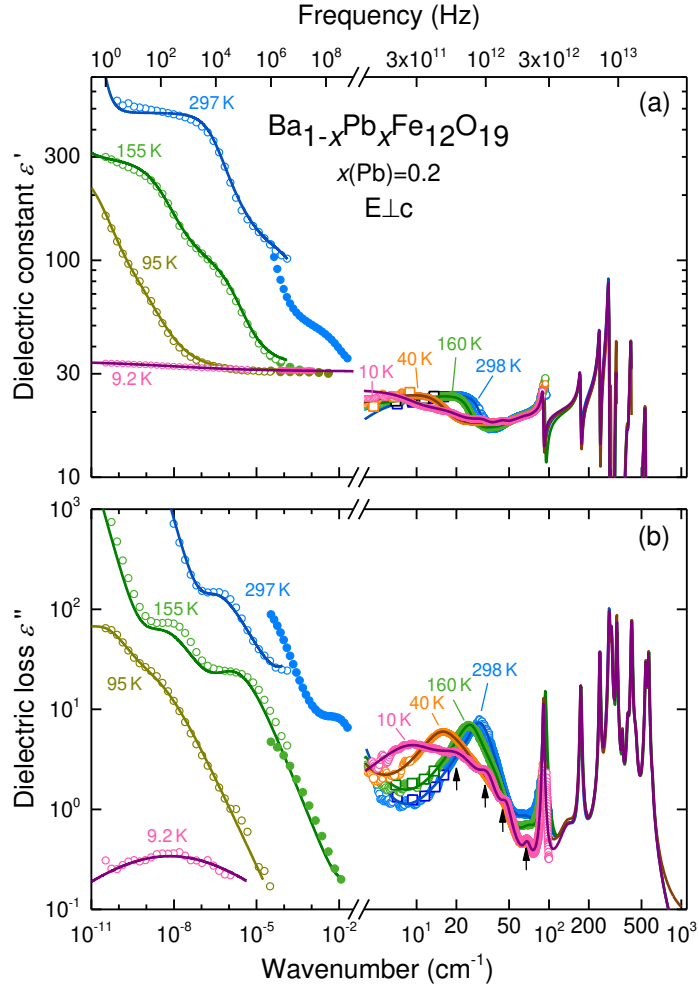


Figure 1. Broad-band (RF-THz-IR) spectra of real (a) and imaginary (b) parts of complex dielectric permittivity of $\text{Ba}_{1-x}\text{Pb}_x\text{Fe}_{12}\text{O}_{19}$, $x=0.2$, measured at selected temperatures for polarization $E \perp c$. Dots correspond to experimental data, lines correspond to results of model processing using Eqs. (1,2) for resonances and overdamped absorptions. Open squares represent the THz data obtained at frequencies of interference maxima in the THz transmission coefficient of the plane-parallel sample, providing an enhanced accuracy in the determination of sample's dielectric parameters²⁴. Four relatively weak absorption lines resolved at 10 K (shown by arrows in panel (b)) correspond to electronic transitions of Fe^{2+} , known also from other Pb-substituted compound $\text{BaFe}_{12}\text{O}_{19}$ ^{23,25–27}. The broad THz absorption band reveals a dramatic frequency softening upon cooling, as it shifts from $\approx 30 \text{ cm}^{-1}$ at 298 K to $\approx 10 \text{ cm}^{-1}$ at 10 K. The symbols below 10^{-2} cm^{-1} represent the results from dielectric spectroscopy at 1 Hz – 300 MHz (open

circles: from the frequency-response analysis; closed circles: from the reflectometric coaxial technique). The marked frequency-temperature dependent response observed at these frequencies is discussed in the text. Note the changes of scale at the frequency axes.

2.2. Radiofrequency and microwave relaxations

Fig. 1 clearly shows that the dielectric response of the $\text{Ba}_{1-x}\text{Pb}_x\text{Fe}_{12}\text{O}_{19}$, $x = 0.2$, compound at low frequencies, 1 Hz to 300 MHz, strongly depends on both frequency and temperature. A similar behavior was found for the $x = 0.1$ compound. The multiple steps in $\epsilon'(\nu)$ and the peaks and shoulders in the $\epsilon''(\nu)$ spectra indicate a rather complex relaxational behavior. The spectra at the highest temperature shown (297 K) reveal a noticeable mismatch between the results from the frequency-response ($\nu \lesssim 1$ MHz; open circles) and those from the reflectometric techniques ($\nu \gtrsim 1$ MHz; closed circles), performed with the different types of electrodes and sample geometries. This points to an extrinsic origin of the relaxations observed at high temperatures²⁸, as discussed in detail below. However, the limiting plateau value of the order of $\epsilon' = 30$, approached at low temperature and high frequencies, should be of intrinsic nature, and it reflects the ionic and electronic polarizability of the material (termed ϵ_∞ in dielectric spectroscopy). Its offset compared to the low-frequency values of the THz data (of order of 20) indicates additional processes occurring in the frequency gap between 10^{-2} and 4 cm^{-1} .

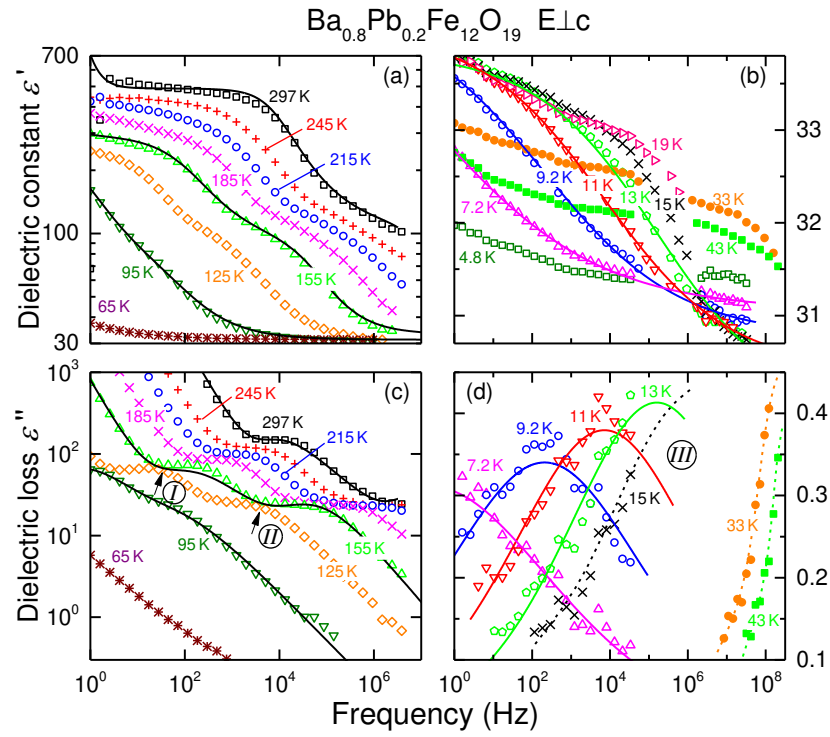


Figure 2. Radiofrequency spectra of the real (a,b) and imaginary (c,d) parts of the dielectric permittivity of $\text{Ba}_{1-x}\text{Pb}_x\text{Fe}_{12}\text{O}_{19}$, $x=0.2$, measured at different temperatures for polarization $E \perp c$. Solid lines represent results of least-square fitting with equation (2). The Roman numerals in circles denote the three relaxational processes clearly visible in this figure. The dashed lines are guides to the eye.

The low-frequency dielectric spectra are shown in more detail in Fig. 2, where it is seen that there are at least three temperature-dependent relaxational processes in the radio- and microwave ranges. Upon cooling from room temperature down to 60–70 K, two relaxational loss peaks (marked as I and II in Fig. 2c) pass through the frequency window of our experiment (1 Hz – 4 MHz), accompanied by the corresponding step-like features in the spectra of the real permittivity $\varepsilon'(\nu)$ (Fig. 2a). A third process (termed III) enters the experimental window when the temperature is lowered down to about 40 K, and it moves outside the window at $T < 7$ K (Figs. 2b and 2d). In contrast to processes I and II (cf. Fig. 1), its behavior as detected by frequency-response analysis (up to about 1 MHz) is consistent with the one detected by the reflectometric technique (beyond 1 MHz, see Fig. 2b), pointing to an intrinsic origin. In the

spectra at $T = 15$ K and 19 K (Fig. 2b), a small additional $\varepsilon'(\nu)$ step is superimposed to the main relaxation at low frequencies. This indicates a fourth process, discussed in more detail below. At 33 K and 43 K, only the low-frequency wings of the loss peaks are detected (Fig. 2d). Employing a closed-cycle refrigerator with shorter coaxial lines allowed for reliable measurements up to about 200 MHz; however, the temperature was limited to 33 K.

The three relaxation features were modeled using the empirical Havriliak-Negami expression for the complex dielectric permittivity (solid lines in Fig. 2):

$$\varepsilon^*(\nu) = \varepsilon'(\nu) + i\varepsilon''(\nu) = \sum_k \frac{\Delta\varepsilon_k}{(1+(i2\pi\nu\tau_k)^{1-\alpha})^\beta} \quad (2)$$

Here $\Delta\varepsilon_k$ is the dielectric strength of the k -th relaxation, τ_k is the mean relaxation time of the relaxation process, and α and β are coefficients describing the broadening and asymmetry of the relaxational spectral response, respectively; their temperature dependences are presented in Fig. SI3-1 in the Supplementary Information. The fits were only performed for temperatures where peak frequencies (in ε'') and/or points on inflection (in ε') could be clearly discerned in the spectra.

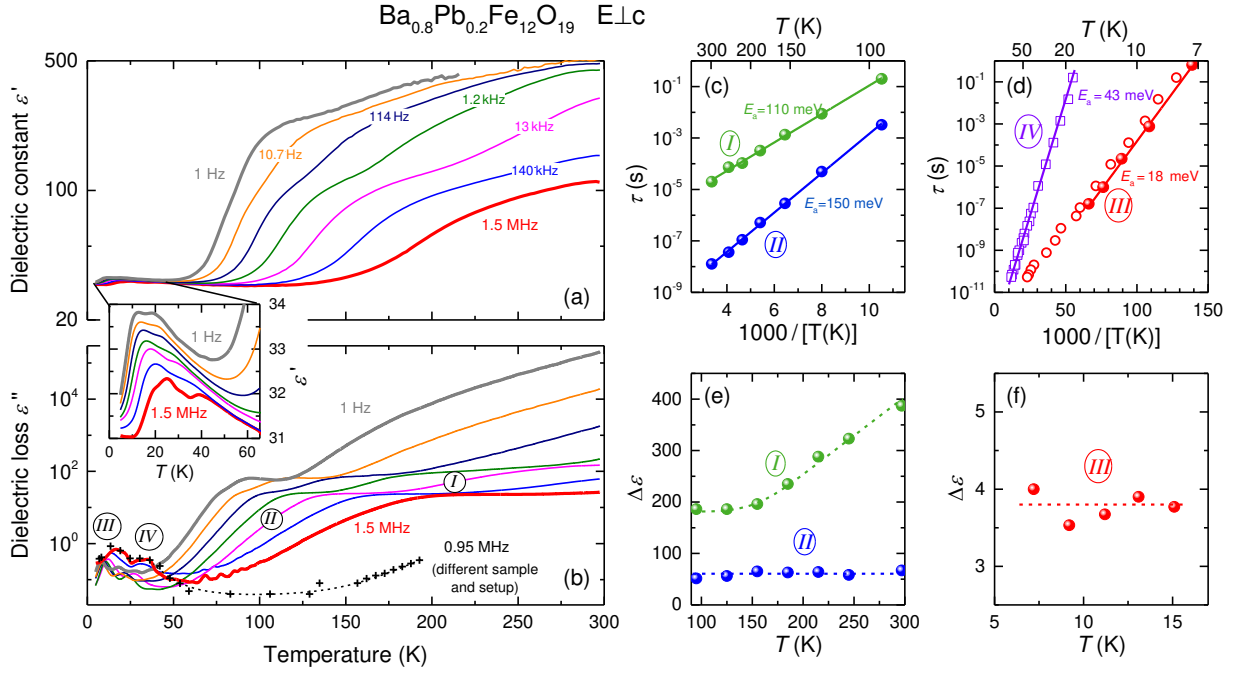


Figure 3. Temperature dependences of the real (a) and imaginary (b) parts of the dielectric permittivity of $\text{Ba}_{1-x}\text{Pb}_x\text{Fe}_{12}\text{O}_{19}$, $x=0.2$, measured for polarization $E \perp c$ at different frequencies (solid lines). The crosses in (b) show results at 0.95 MHz as measured in a different setup and for a sample with different geometry and electrodes. The Roman numerals denote the four detected relaxation processes (extrinsic: I and II; intrinsic: III and IV). The comparison between the data obtained on different samples utilizing different setups clearly illustrates the intrinsic character of the relaxations III and IV (see text). Panels c, d show Arrhenius plots of the temperature dependences of the relaxation times that correspond to the relaxational excitations observed in the low-frequency complex dielectric permittivity spectra of $\text{Ba}_{1-x}\text{Pb}_x\text{Fe}_{12}\text{O}_{19}$ with $x=0.2$. The values correspond to the four peaks I - IV, seen in the $\varepsilon''(\nu, T)$ data (panel b and Fig. 2). The closed spheres were deduced from fits of the $\varepsilon''(\nu)$ and $\varepsilon'(\nu)$ spectra (Fig. 2), whereas the open symbols were derived from the temperature-dependent data of panel b and Fig. SI3-2, which only provided an estimate of τ . The straight lines evidence a temperature activated behavior with the activation energies as indicated. The temperature dependences of the dielectric strengths of relaxations I - III are shown in panels e and f. The dashed lines are guides to the eye.

The relaxation processes are often revealed more clearly in temperature-dependent plots of the permittivity, especially if the relaxations appear close to the device operation limit as it is, e.g., the case for process III (cf. Fig. 2d). Figure 3 (a), (b) displays the temperature dependences of the real ε' and imaginary ε'' parts of the dielectric permittivity measured at various fixed frequencies (solid lines). These plots reveal four pronounced anomalies with shapes typical of relaxational processes (peaks in ε'' and steps in ε'). Their frequency-dependent character is better visible in a plot of the temperature-dependent AC conductivity $\sigma'(T)$ (Fig. SI3-2) where the different curves exhibit less overlap due to the offset caused by the relation $\sigma'(T) \sim \nu \varepsilon''(T)$. The inset of Fig. 3b provides a magnified view of $\varepsilon'(T)$ for the two low-temperature relaxations, revealing a weak but significant increase in their static real permittivity with decreasing temperature, in accord with the temperature-dependent static dielectric constant becoming obvious in Fig. 2b. Comparing the frequencies and temperatures of the occurrence of these four processes with those in Fig. 2, three of them can be clearly identified with the relaxations I, II and III, discussed above. The features emerge when, during cooling, the relaxational peaks in $\varepsilon''(\nu)$ and the corresponding points of inflection in the $\varepsilon'(\nu)$ spectra of processes I, II, and III shown in Fig. 2 move into the measurement frequency interval. Interestingly, in Fig. 3, a weak additional process (IV) is detected located between about 20 and 40 K, and depending on frequency. We note that the temperature-dependent plots in Fig. 3 point to the absence of any phase transition at low temperatures down to $T \approx 2$ K, which is also evident from the smooth temperature dependence of the specific heat, see Fig. SI4-1 in the Supplementary Information.

The pluses in Fig. 3b represent $\varepsilon''(T)$ results for 0.95 MHz as measured independently in a special experimental setup* for another sample with different geometry and contacts. The agreement in the region of relaxations III and IV clearly points to their intrinsic origin. In contrast, marked differences in the region of the high-temperature relaxations I and II are observed, which we also found for various other measurements, performed with different setups

* Using a Janis He-flow cryostat in Prague instead of the Cryovac He-bath cryostat in Augsburg.

and for various samples with particular types of electrodes. As already suggested above based on Fig. 1, this proves the extrinsic, most likely contact-related origin of these processes. It is well known that extrinsic, so-called Maxwell-Wagner relaxations can arise, e.g., due to the formation of Schottky barriers at the sample-electrode interfaces, which leads to deviations as observed in the present case²⁸.

The temperature-dependent results of Fig. 3 (and in Fig.SI3-2) provide an additional way to estimate relaxation times as a function of temperature by determining the loss-peak temperatures T_p for a given measurements frequency ν . For $T = T_p$, the relaxation time is given by $\tau(T)=1/(2\pi\nu)$. This enables an extension of the covered temperature and frequency range for $\tau(T)$, albeit with a somewhat reduced precision compared with the relaxation times deduced from fits of the frequency-dependent data (Figs. 1 and 2). Figs. 3c and 3d give an Arrhenius presentation of the relaxation times τ of the four detected processes. The $\tau(T)$ data follow an activated behavior with four activation energies, 110 meV (process I), 150 meV (process II), 18 meV (process III), and 43 meV (process IV). According to Figs. 3e and 3f, the dielectric strengths $\Delta\epsilon$ of relaxations II and III do not change with temperature in the shown temperature intervals. The dielectric strength of relaxation I reveals a strong decrease upon cooling down to 150 K, but it levels off at lower temperatures. The dielectric strength of process IV is too weak to allow for any unequivocal determination of its temperature dependence. The $\Delta\epsilon$ results for process III (Fig. 3f) are also of limited precision because of the superimposed contribution of process IV which was not considered in the fits. Whereas relaxations I and II are extrinsic, the intrinsic relaxations III and IV might manifests the dynamical response of dielectric or magnetic domains, similar to a related compound with higher concentration of Pb, $\text{Ba}_{0.3}\text{Pb}_{0.7}\text{Fe}_{12}\text{O}_{19}$ ²³. In that compound, pronounced dielectric and magnetic relaxational dynamics were detected in the radio frequency range; both relaxations exhibit similar characteristic relaxation times, evidencing the bi-relaxor-like nature of $\text{Ba}_{0.3}\text{Pb}_{0.7}\text{Fe}_{12}\text{O}_{19}$ ²³. Our magnetic/electrostatic force microscopy experiments clearly indicate the presence of magnetic domains in pure BaM (Fig.SI5-1, SI5-2,

SI5-3 in Supplementary Information). Thus, the relaxation-like dispersion we observe in the magnetic permeability spectra of $\text{Ba}_{0.8}\text{Pb}_{0.2}\text{Fe}_{12}\text{O}_{19}$ (Fig.SI6-1) should be associated with magnetic domains dynamics. As to the *dielectric* relaxations III and IV, we suggest that their origin should be related to the response of magnetic domain walls, which are electrically polar in the present compound. The mechanism of emergence of electric polarization in magnetic domains walls is analyzed in ²⁹ taking iron garnet as an example. We firmly detect the electrical polarity at the boundaries of magnetic domains in undoped BaM (Fig.SI5-2). At the same time, in the Pb-doped $\text{Ba}_{0.8}\text{Pb}_{0.2}\text{Fe}_{12}\text{O}_{19}$, along with the clearly visible magnetic domain structure (Fig.SI5-3), we were not able to detect any sign of the domain polarity, that is most probably beyond the sensitivity of the used technique. This last suggestion is confirmed by the low values of dielectric strengths of the two relaxations, III and IV, $\Delta\epsilon \ll 10$, which is by orders of magnitude less than those seen in pure BaM ($\Delta\epsilon \approx 1000$) ²³. We also note a considerable difference in activation energies of these relaxations, 18 meV (III) and 43 meV (IV).

2.3. Gigahertz resonances

Although our experiments did not cover the spectral range between several GHz and ~100 GHz, our measurements indicate that some excitations exist in this frequency interval. First of all, this is evidenced by a “step” in the spectra of the real permittivity between the radio- and THz frequencies, as seen in Fig. 1a. In addition, below 20 cm^{-1} , there is a clear decrease in the real part of permittivity $\epsilon'(\nu)$ and, below 10 cm^{-1} , an increase in its imaginary part $\epsilon''(\nu)$ (see Fig.SI7-1). Both these features are linked together, and they strongly suggest the existence of a resonant absorption band located below 3 cm^{-1} (90 GHz). Assuming its purely dielectric nature, we were able to apply expression (1) to model its spectral response with a dielectric Lorentzian, which let us estimate the values and the temperature dependences of its parameters. Examples of the corresponding least-square fits of the room-temperature spectra are given in Fig.SI7-1. As demonstrated in Fig.SI7-2, there are no strong changes with temperature in the frequency position and damping parameter of the excitation; also, its dielectric and oscillator strengths

show signs of decrease on cooling. Note that the dielectric strength of the resonance practically matches the “step” between the radiofrequency and THz values of real permittivity (Fig.1a), signifying there are no additional absorption bands except the one at 2-3 cm^{-1} in the range. As for the microscopic origin of the detected GHz band, we cannot exclude that it can be of mixed magneto-electric origin^{30,31}. Some evidence for that is given by the coincidence (within experimental uncertainties) of its frequency position with the value of the frequency of ferromagnetic resonance in the $\text{Ba}_{0.9}\text{Pb}_{0.1}\text{Fe}_{12}\text{O}_{19}$ crystal obtained by extrapolation of the magnetic field-dependent frequency of the resonance to zero magnetic field (Fig.SI8-1).

2.4. THz spectra, the soft mode

The most intriguing result of the present study is the observation of an excitation at THz frequencies whose frequency position and dielectric strength reveal strong changes when the temperature is varied, as seen in the THz (5-70 cm^{-1}) spectra of $\epsilon'(\nu)$ and $\epsilon''(\nu)$ in Fig. 1. Fig. 4 (a,b) demonstrates that in the $x=0.1$ compound, a drastic change in the resonance frequency position of the soft mode occurs (panel a) that strongly contrasts with the temperature-independent behavior of the position of the lowest-frequency optical phonon at 92 cm^{-1} (panel b). Before discussing the behavior and the origin of the soft excitation in more detail, we comment on four narrower absorption lines that are resolved at the lowest temperatures on the high-frequency wing of the excitation; they are marked by arrows in Fig. 1. Comparing frequency positions, intensities and temperature evolution of these lines with those seen in the THz spectra of isostructural compounds, i.e., in $\text{Ba}_{1-x}\text{Pb}_x\text{Fe}_{12}\text{O}_{19}$ with $x=0.7$ ²³, $x=0.6$ and 0.8 ^{25,27}, we conclude that the four resonances observed in $\text{Ba}_{1-x}\text{Pb}_x\text{Fe}_{12}\text{O}_{19}$ with $x=0.1$ ($x=0.2$) at 64 (68), 47 (48), 34 (34), 22 (21) cm^{-1} have the same origin. We associate these resonances with electronic transitions between the fine-structure components of the ^5E ground state of tetrahedrally coordinated Fe^{2+} . The presence of Fe^{2+} ions in BaM and in Pb-substituted BaM is due to both growth defects (mainly oxygen vacancies) and sharing the outer $6s^2$ electron pair of Pb with the Fe^{3+} ion. A similar effect was observed in Ti^{4+} -substituted hexaferrites³², where Fe^{2+} ions

maintain the charge neutrality of the compound with aliovalent doping. In addition, in Ti-substituted BaM ($\text{BaTi}_{0.75}\text{Fe}_{11.25}\text{O}_{19}$)²⁰, calculations of the adiabatic potential showed that for Fe^{2+} in BaM matrix, it is the tetrahedral coordination that is most energetically favorable. We note that the intensities of the lines are higher in the $x=0.2$ $\text{Ba}_{1-x}\text{Pb}_x\text{Fe}_{12}\text{O}_{19}$ compound compared to the compound with $x=0.1$, which is in agreement with our assumption on the nature of these absorption lines due to the presence of the Pb^{2+} ions.

To find out whether some magnetic excitation can be at the origin of the discovered THz soft mode, similar to Y- and Z-type hexaferrites^{33,34}, we performed THz spectral measurements in external magnetic fields of up to 7 T (Faraday geometry) at temperatures 4-300 K. No influence of the magnetic field on the spectra was detected, indicating a purely dielectric nature of the soft excitations in both $x=0.1$ and $x=0.2$ compounds. An additional confirmation of their dielectric origin is provided by the shape of the reflection coefficient spectrum, as demonstrated and discussed in the Supplementary Information SI9 and illustrated in Fig. SI9-1. This justifies the use of the dielectric Lorentzian expression (1) for least-square processing of the THz spectra $\epsilon'(\nu)$ and $\epsilon''(\nu)$, in order to obtain parameters of the soft modes observed in both $\text{Ba}_{1-x}\text{Pb}_x\text{Fe}_{12}\text{O}_{19}$ samples, $x=0.1$ and $x=0.2$. Temperature dependences of these parameters (dielectric strength $\Delta\epsilon$, peak frequency ν , damping γ and oscillator strength $\Delta\epsilon\nu^2$) for both compounds are presented in Figure 4 (c-f). Note that the modes are not of relaxational but of resonance type, which is evidenced by the dispersion in the real permittivity $\epsilon'(\nu)$, typical of underdamped excitations, and by the small relative damping values, $\gamma/\nu < 1$. The frequency positions of the modes in both compounds nearly coincide, and they reveal significant decreases upon cooling down, from ≈ 30 cm^{-1} at room temperature to ≈ 10 cm^{-1} at 10 K, see Fig. 4d. This softening of the frequency is accompanied by a strong increase in the dielectric strengths $\Delta\epsilon$ that differ slightly in the two materials.

The dependences of the resonance frequency positions $\nu(T)$ and dielectric strengths $\Delta\epsilon(T)$ of the excitations resemble the temperature behavior of ferroelectric soft modes originating in

structural phase transitions in ferroelectric materials^{35,36}. However, in the present case, the $\nu(T)$ and $\Delta\varepsilon(T)$ temperature evolutions do not obey the corresponding Cochran, $\nu^2 = A(T - T_C)$, and Curie-Weiss, $\Delta\varepsilon = C(T - T_C)^{-1}$, laws (T_C – Curie temperature, A – Cochran constant, C – Curie constant), typical of ferroelectrics. Instead, the temperature behavior of the resonance frequencies clearly follows power-law dependences

$$\nu^2 = A(T - T_C)^\delta \quad (3)$$

with the best fit parameters $\delta = 0.5 - 0.6$ and critical temperatures $T_C \approx 3.3$ K for $x=0.1$ and $T_C \approx 1.5$ K for $x=0.2$ compounds. In addition, the damping constants remain, within the experimental uncertainty, temperature-independent in the entire temperature range; this is also unusual for “standard” ferroelectric soft modes. One more feature of the soft excitations observed in the $\text{Ba}_{1-x}\text{Pb}_x\text{Fe}_{12}\text{O}_{19}$ compounds should be pointed out: the oscillator strengths strongly decrease as the temperature is lowered (Fig. 4f), which is in strong contrast to regular ferroelectrics where the soft modes usually maintain their oscillator strengths constant with temperature. Such a weakening could occur if the excitation were coupled to an additional vibrational process. Since no noticeable change with temperature in the total dielectric contributions of all IR-active phonons (Fig. 1a) were detected, the strengths of the soft modes might be transferred to the lower-frequency gigahertz resonance seen in Fig. SI7-1. Unfortunately, parameters of this resonance could be only determined from the data extrapolated from THz and radio-frequency ranges, and, consequently, its oscillator strength is found with a rather large uncertainty. Nevertheless, it is clearly seen from Fig. SI7-2d, that the excitation strength does not show any sign of increase upon cooling. Therefore, we exclude its coupling to the soft mode. Further detailed microwave dielectric measurements are required in order to gain additional information on this resonance.

It should be noted that the E_{1u} -symmetry modes are observed for polarization $E \perp c$, i.e. when the electric field component of the probing THz radiation couples to the electric dipole moments that exist within the ab -plane. Previous studies on hexaferrites revealed temperature-dependent excitations in another geometry, $E \parallel c$. For example, in ²¹, a soft excitation and the corresponding incipient ferroelectric temperature behavior of the low-frequency dielectric permittivity had been observed in undoped BaM in the $E \parallel c$ response, with no indications of any soft-mode-like effects in the orthogonal polarization $E \perp c$, as in the present case.

The observed peculiar temperature dependence of the THz soft mode frequency seen in the $E \perp c$ spectra of $\text{Ba}_{1-x}\text{Pb}_x\text{Fe}_{12}\text{O}_{19}$ could be associated with the response of Fe(2) ions that oscillate in a quartic potential within the ab -plane, as discussed in Supplementary Information, section SI10 (see also Fig.SI10-1). These ions lie in the same plane as Ba/Pb ions, and they can be affected by the nearest Pb ions that substitute Ba. However, as is shown in SI10 section of Supplementary Information, the calculated AC conductivity that characterizes the absorption related to Fe(2) vibration becomes larger at low temperature, in strong contrast to the present experiment.

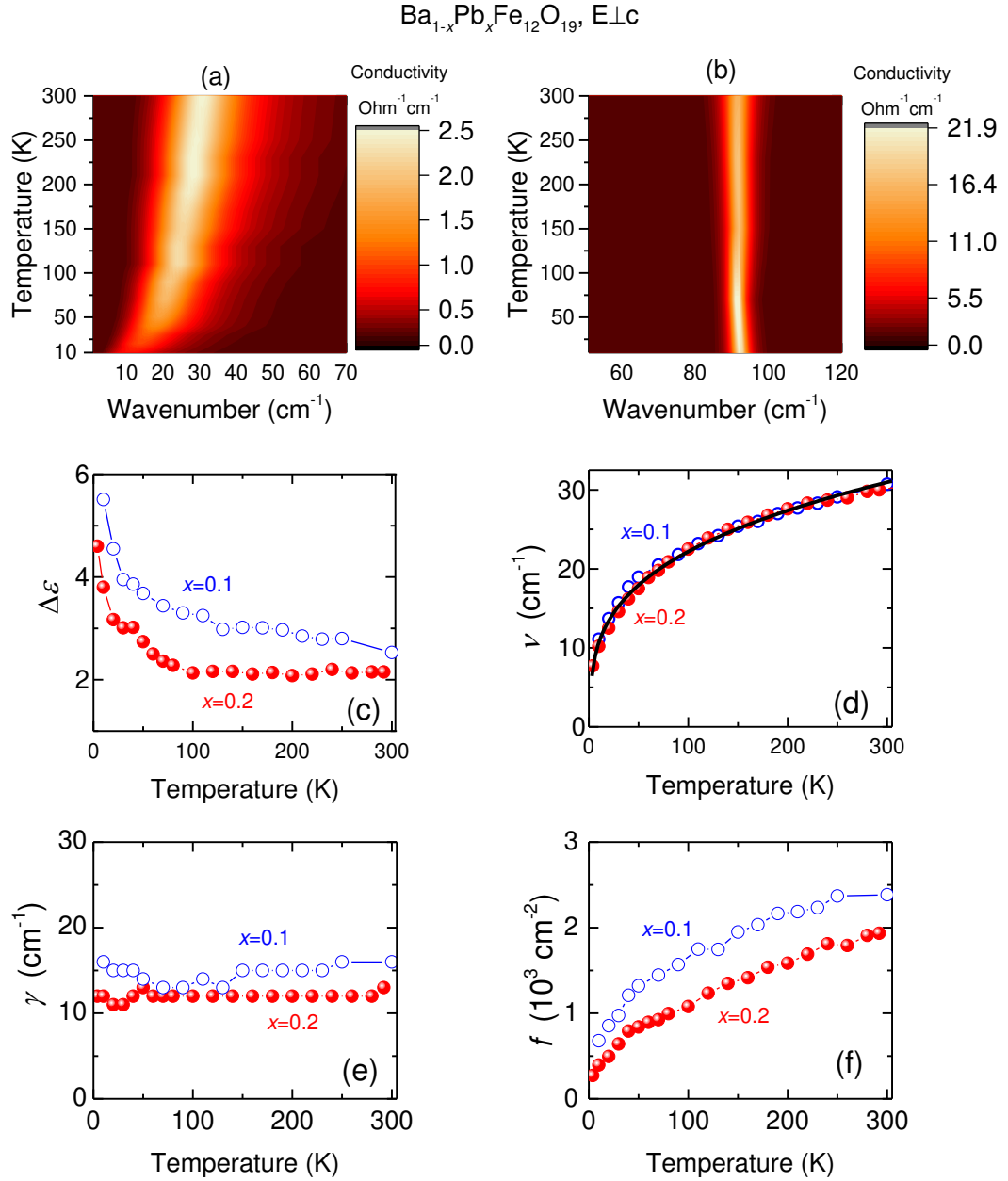


Figure 4. 2D plots of temperature-dependent spectra of the real part of AC conductivity of the THz soft excitation (a) and the lowest E_{1u} optical phonon (b) for the $\text{Ba}_{1-x}\text{Pb}_x\text{Fe}_{12}\text{O}_{19}$ crystal, $x=0.1$. Panels (c-f): parameters of the soft THz excitation as a function of temperature for $\text{Ba}_{1-x}\text{Pb}_x\text{Fe}_{12}\text{O}_{19}$, $x=0.1$ and $x=0.2$ crystals: dielectric strength (c), resonance frequency (d), damping factor (e) and oscillator strength (f). Black line in the panel (d) shows a fit of the resonance frequency for $x=0.1$ with the power-law dependence $\nu^2 = A(T - T_c)^\delta$, yielding $\delta=0.5-0.6$, $T_c \approx 3.3$ K.

We suggest the following mechanisms of emergence of an *ab*-plane dipole moment and of the soft mode in Pb-doped hexaferrites. In the hexaferrite lattice, the Ba cuboctahedron is symmetrically surrounded by three bipyramids. The Ba ions occupy central positions in the oxygen cuboctahedra with six oxygen ions surrounding each Ba ion in the *ab*-plane (Fig.SI2-1b, top). When Ba is substituted with Pb, the interaction of the lone $6s^2$ electron pair of the Pb^{2+} with neighboring oxygens leads to shortening of Pb-O bonds²², in comparison to Ba-O bonds³⁷, that manifests itself in an off-center shift of Pb^{2+} towards one of the oxygen vertices²² (Fig.SI2-1b, bottom). This, in turn, leads to a distortion of the ionic surrounding, redistribution of electron density and appearance of a net electric dipole moment in the *ab*-plane. (If the Pb ion were located in the center of its oxygen coordination, the dipole moments induced in the three surrounding trigonal bipyramids would compensate each other and the net dipole moment would be zero). Since the Pb ion is surrounded by six oxygens, at low enough temperature it can find itself in one of six local minima within the *ab*-plane.

At high enough temperatures, the Pb ion will be able to hop between the six potential wells which can be effectively regarded as if the corresponding induced dipole moment changed its direction during whole 360 degrees rotation within the *ab*-plane. Due to the long-range character of the electric dipole-dipole interaction, separate dipoles of the described type will interact, with the tendency towards ordering at certain low temperature, as it happens in paraelectric phases of ferroelectrics. One can expect that the dielectric response of such coupled dipolar systems can be expressed in the form of soft excitation analogous to the paraelectric soft modes in systems with a crossover from displacive to order-disorder type of ferroelectric phase transition (see, e.g.,^{35,36}). When the temperature decreases and the thermal energy $k_B T$ becomes smaller than the energy barriers A between the potential wells (here k_B is the Boltzmann constant), a certain fraction of the Pb ions progressively resides in the wells, and the fraction of quasi-free dipoles becomes smaller in accordance with the Boltzmann exponential factor $\exp(-A/k_B T)$. The

dielectric response of such kind of system of coupled rotating electric dipoles was analyzed within the mean-field approach in ³⁸ and ³⁹ for the rotational potential felt by a dipole containing two and four potential minima, respectively. According to ³⁸, for the case of the potential with two wells, at high temperatures, when the thermal energy exceeds the barrier height A separating the wells ($k_B T > A$), there will be an optical soft mode in the dielectric spectra that originates in freely interacting rotating dipoles. During cooling, the number of these dipoles that are responsible for the soft mode-like response will decrease proportionally to the Boltzmann exponent $\exp(-A/k_B T)$ and, correspondingly, progressively more dipoles will be localized within the wells and respond via librations (restricted rotations) to external perturbations. Depending on the coupling strength and barrier height, the soft-mode dielectric strength $\Delta\varepsilon$ (its contribution to the static permittivity) can either follow the Curie-Weiss dependence $\Delta\varepsilon = C(T-T_C)^\gamma$, $\gamma = -1$, or exhibit certain deviations from it towards lower absolute values of the exponent, $|\gamma| \leq 1$. Along with that, the temperature dependence of the soft mode frequency is also expected to reveal deviations from the Cochran law $\nu^2 = A(T - T_C)$, as demonstrated in ⁴⁰ for the case of interacting classical anharmonic oscillators in the two-well potential. Since the above-mentioned mean-field results predict the existence of the two principal features we observe in our experiments - the soft mode and the decrease in its strength upon cooling, we suggest that the described considerations can be qualitatively applied to our case when the rotating dipoles are produced by Pb ions experiencing the six-well potential. It is worth noting that the described model was effectively used to interpret the paraelectric response of isolated nano-confined polar water molecules embedded in beryl crystals ⁴¹.

Note also that other factors can add to the observed exotic temperature variations of the soft-mode frequencies and dielectric strengths, for instance the rather complex structure of the studied compounds. Such complexity can make the soft mode couple to the magnetic subsystem (the possibility of spin-phonon coupling in hexaferrites has been reported in, e.g. ^{9,42-46}). Also, we cannot exclude a coupling between the soft mode and the transitions within fine-structure

components of the 5E ground state of tetrahedrally coordinated Fe^{2+} , since the frequencies of both types of excitations are close or even overlap, as discussed above (see Fig. 1).

One more aspect should be considered for the physics of the studied hexaferrites: there are indications that quantum critical phenomena can play significant role in their dynamical properties. First principles calculation along with Monte-Carlo simulations using dipole-dipole interaction model ⁷ indicate the possibility of a phase transition in BaM at $T_c=3$ K into a geometrically frustrated anti-ferroelectric state. Kumar and Pandey ⁴⁷ claimed an observation of a phase transition in Ca-substituted BaM at similar temperatures. They showed that the temperature of the phase transition rises with the concentration of the dopant in a manner characteristic for the phase transitions in a quantum critical regime. Ca^{2+} generates a positive chemical pressure within the BaM matrix, and as a result, it leads to a decrease in the unit cell parameters. The rise of the transition temperature T_c is connected with an increasing dipole-dipole interaction strength in and out of the *ab*-plane with shortening of bonds in the trigonal bipyramids due to effect of positive chemical pressure. Accordingly, the positive chemical pressure can stabilize a quantum electric dipolar glass state and drive the system away from the quantum critical point ⁴⁷. It was further predicted that a negative chemical pressure should decrease the critical temperature of the transition and bring the substituted BaM closer to the quantum critical point. The negative chemical pressure can be produced in BaM matrix by substitution of Ba^{2+} with Pb^{2+} , resulting in $Ba_{1-x}Pb_xFe_{12}O_{19}$ materials studied here. According to our X-ray analysis (see Section S1 in Supplemental Information), addition of the Pb^{2+} favors an expansion of the *ab*-face in the unit cell of the $Ba_{1-x}Pb_xFe_{12}O_{19}$ compounds, indicating that Pb^{2+} generates a negative chemical pressure indeed. When modeling the temperature dependences of the THz soft-mode frequency by Eq.3, the critical temperature T_c is lower in the compound with larger content of Pb^{2+} , in agreement with suggestions of Kumar and Pandey ⁴⁷. Rowley et al. ⁴⁸ found an evidence of proximity of pure hexaferrites BaM and $SrFe_{12}O_{19}$ to the quantum critical point, which was indicated by a pronounced rise in the dielectric permittivity upon cooling. They

also showed that though pure BaM is expected to change its phase from paraelectric to antiferroelectric one at around 6 K, this transition is suppressed due to quantum fluctuations and does not occur at finite temperature. Evidence of existence of quantum paraelectric phases in M-type hexaferrites was reported also in ^{7,12,13,47}.

With the above taken into account, we consider the THz soft mode observed in the studied compounds as a possible fingerprint of a (quantum) phase transition that could happen in $\text{Ba}_{1-x}\text{Pb}_x\text{Fe}_{12}\text{O}_{19}$, if not suppressed by quantum fluctuations, below the lowest temperatures of 4 K used in our experiments. It might be that doping with Pb destabilizes the coupled spin-phonon system in the material and brings it close to a quantum phase transition that can be driven by Pb doping, where the critical concentration can be close to $x(\text{Pb}) = 0.2$. This is evidenced by the critical temperatures obtained by fitting our data using Eq.3, yielding a decrease from $T_c \approx 3.3$ K for $x = 0.1$ to $T_c \approx 1.5$ K for $x = 0.2$. It is known that in the critical temperature region around the phase transition, when quantum effects come into play, the inverse dielectric constant of the corresponding soft excitation obeys a power law $(\Delta\varepsilon)^{-1} \sim T^\gamma$ with a critical exponent $\gamma = 2$ for multi-axial dipole orientations when polarization is confined to change along any direction ⁴⁹⁻⁵¹. Because we could not determine the soft mode dielectric strength precisely enough, we cannot make a firm conclusion on this theoretical prediction in the case of our hexaferrites. To clarify this matter, systematic and more detailed investigations on the spectroscopic properties of $\text{Ba}_{1-x}\text{Pb}_x\text{Fe}_{12}\text{O}_{19}$ crystals with series of $x(\text{Pb})$ and in both polarizations, $E \perp c$ and $E \parallel c$, are in progress.

3. Conclusions and prospects

Our thorough spectroscopic study of the broad-band (1 Hz up to 240 THz) temperature-dependent (5 K – 300 K) electromagnetic properties of $\text{Ba}_{1-x}\text{Pb}_x\text{Fe}_{12}\text{O}_{19}$ single crystals found a rich variety of strongly temperature- and doping-dependent electric, magnetic and possibly magneto-electric excitations. Most intriguing from both fundamental and applied points of view is

the complex electromagnetic response of the compounds at THz frequencies that is found to be determined by electronic transitions between the fine-structure components of the 5E ground state of tetrahedrally coordinated Fe^{2+} ions which overlap with a soft excitation whose temperature evolution resembles that of a ferroelectric soft mode. A close inspection shows, however, that the temperature dependences of the resonance frequency and strength do not follow the corresponding Cochran and Curie-Weiss laws known to describe soft modes in classical ferroelectrics. We proposed a microscopic model that qualitatively explains the observed behavior of the excitation. It was shown that the radiofrequency electrodynamic characteristics of the studied compounds are fully determined by relaxational processes that are related to the Maxwell-Wagner polarization and to the dynamics of magnetic domain walls. Summarizing, our findings provide hints at the understanding of the physics that is behind the radiofrequency, THz up to the IR electromagnetic response of the studied hexaferrites.

Being planar, self-biased and low-loss materials, hexaferrites meet the requirements of modern microwave and THz circulators, phase-shifters, filters, isolators and millimeter wave resonators antennas^{15,16,30,52}. The fact that these compounds are considered nowadays as one of the most promising material classes for telecommunication systems has been clearly demonstrated in a recent work^[42]. Here, $BaFe_{12}O_{19}$ /polydimethylsiloxane nanocomposite that exhibits a zero-bias (no external magnetic field) ferromagnetic resonance frequency at 46.6 GHz is proposed for the design of a circulator with operating frequency of 35 GHz. The absorption resonances at even higher frequencies of ≈ 50 and ≈ 100 GHz that we discovered in single crystalline Pb-doped hexaferrites $Ba_{1-x}Pb_xFe_{12}O_{19}$ make these compounds promising candidates for manufacturing self-biased devices with working frequencies meeting standards of the higher generations in telecommunications. Considerations of the possibilities of purposeful tuning of the resonance frequency with dopant content x or (moderate) external magnetic fields are in progress, as well as the characterization of ceramic, sputtered films and nanocomposite forms of the compounds. One of the most significant results of the present work is that we present quantitative

information on the electrodynamic properties of hexaferrites in an extremely wide frequency range, including bands that are most attractive from the viewpoint of the development of next-generation communication systems. We have also revealed the fundamental physical mechanisms that determine these properties. Such information will allow a most effective approach to the use of hexaferrites for manufacturing components of microwave and THz electronics. With a rich structure of electronic transitions overlapping with the soft THz resonance one could think of the opportunity to build a long-wavelength laser operating in the millimeter wave region. The presence of the detected strongly temperature-dependent THz absorption band opens the way to fabricate THz tunable electronic components, such as band-stop filters, phase-shifters and attenuators, surpassing existing analogues in their characteristics^{30,53,54}. Taking into account the multiferroic properties of the barium hexaferrites⁵⁵⁻⁵⁷, the area of their possible applications can expand remarkably.

4. Methods

Sample preparation: Single crystals of Pb-substituted barium hexaferrite with chemical compositions $\text{Ba}_{1-x}\text{Pb}_x\text{Fe}_{12}\text{O}_{19}$ ($x = 0.1$ and 0.2) were grown using the flux method. Crystal growth and characterization are described in Section SII of Supplemental Information. For spectroscopic THz and IR measurements, the crystals were carefully oriented (see section SII in Supplemental Information) and then prepared as plane-parallel (to within few micrometers) plates with the crystallographic c -axis oriented perpendicular to plates surfaces; this geometry allowed for measurements with the linear polarization of the electric field \mathbf{E} -vector of the probing radiation lying within the ab -planes, $E \perp c$. Both sides of the prepared plates were carefully polished with diamond lapping films in order to meet the requirements of THz-IR measurements. Sizes of the samples for THz and IR measurements were about 3 mm x 4 mm with thicknesses of 335 μm ($x=0.1$) and 452 μm ($x=0.2$). For measurements at frequencies from 1 Hz up to the microwave range (1 GHz), specimens were fabricated as thin plane-parallel

polished plates with thicknesses of 174 μm (Augsburg) and 758 μm (Prague) with the c -axis parallel to the plate surfaces, thus allowing for measurements in the $E \perp c$ geometry.

Terahertz-infrared spectroscopy: Experiments in the THz range (at frequencies $\nu=8\text{--}100\text{ cm}^{-1}$, 0.24–3 THz) were conducted with the help of two time-domain spectrometers, Menlo Tera K15 and TeraView TPS 3000. Spectra of complex transmission coefficient (amplitude and phase) of the plane-parallel samples were measured, and the spectra of complex dielectric permittivity $\varepsilon^*(\nu)=\varepsilon'(\nu)+i\varepsilon''(\nu)$ were calculated using standard Fresnel equations⁵⁸. In the far-IR and mid-IR spectral regions (30–8000 cm^{-1} , 0.9–240 THz), a standard Fourier-transform spectrometer Bruker Vertex 80 was utilized for the measurements of reflectivity spectra. For measuring reflectivity at the lowest frequencies (25 to 80 cm^{-1}), a Fourier-transform spectrometer Bruker 113v with helium-cooled bolometer was used. The experiments were done in a wide range of temperatures (5–300 K) using exchange-gas and cold-finger cryostats. For the experiments in external magnetic fields of up to 7 T, Spectromag Oxford cryomagnets attached to a Fourier-transform IR spectrometer Bruker 113v and to a custom-made time-domain THz spectrometer were employed.

Radio frequency impedance spectroscopy: At frequencies from $\approx 1\text{ Hz}$ to $\approx 200\text{ MHz}$ and at temperatures from 5 K to 300 K, the dielectric response of the samples was measured using a Novocontrol Alpha frequency-response analyzer and a Keysight 4991B impedance analyzer. For cooling, a closed-cycle refrigerator (CTI-Cryogenics), a He-flow cryostat (JANIS ST-100), and a He-bath cryostat (Cryovac) were used. For the measurements at frequencies of up to about 4 MHz, Pt-Au-electrodes were evaporated using a Bal-Tex SCD 050 sputter coater onto the principal faces of the samples, or silver paste layers were directly applied as electrodes. The connections for applying the AC electric field were provided by silver or copper wires fixed to the electrodes by silver paste. For frequencies above about 1 MHz, a coaxial reflectometric setup was used, employing the impedance analyzer as described in⁵⁹. Here the sample was mounted between two metal plates at the end of a coaxial line. Depending on the used cooling devices, the

dielectric response of the samples was measured in vacuum or helium atmospheres, which did not significantly influence the measured dielectric properties. The precise determination of absolute values of the complex dielectric permittivity is hampered by the occurrence of stray capacitances and geometrical uncertainties which play a role especially for rather small single crystals as investigated in the present work. For the frequency-response measurements below about 4 MHz, the largest samples were available. Here, different samples with different geometries and contact configurations were independently measured by the Prague and Augsburg groups, yielding comparable absolute values in the frequency/temperature ranges dominated by intrinsic effects. The less precise high-frequency results obtained by the reflectometric method were scaled to the low-frequency results by a single factor for all data obtained during a measurement run.

Heat capacity measurements: The temperature dependence of the heat capacity c_p was measured (via the standard relaxation method) using the heat capacity option of the Physical Property Measurement System (Quantum Design).

Magnetic Force microscopy: With the scanning probe microscopy, we have investigated two samples, $\text{BaFe}_{12}\text{O}_{19}$ and $\text{Ba}_{1-x}\text{Pb}_x\text{Fe}_{12}\text{O}_{19}$ ($x=0.2$), in order to prove the multiferroic nature of the crystals. We used magnetic force microscopy to observe the magnetic domain structure under low temperature (4.5 K) and ambient conditions. For low-temperature measurements, the AttoDRY 1000 system with a possibility to apply magnetic field was used. For room-temperature investigations we have used the NT-MDT AFM device. These magnetic force measurements were done with a Bruker MESP-V2 cantilever. Both crystals show similar domain structure with negligible temperature dependences, and a clear magnetic response to the external magnetic field. After that we have used a conductive (PtIr coated, Bruker) cantilever to check the electrostatic response of the samples. In BaM, an electrostatic polarization of magnetic domains boundaries is clearly observed, whereas in the Pb-doped crystal, no such effect was detected.

Acknowledgements

Authors are grateful to Professor A. Mukhin and Professor G. Komandin for fruitful discussions. The THz cryogenic study was supported by the Russian Science Foundation, grant 19-72-00055; IR measurement were supported by the Russian Foundation for Basic Research, grant 20-32-90034, LNA acknowledges support of the Russian Ministry of Higher Education and Science, state contract 1740-20 and system of President's scholarships for young researchers (SP-777.2021.5). Czech coauthors were supported by the Czech Science Foundation (Project No. 21-06802S) and by the MŠMT Projects LM2018096 and SOLID21 - CZ.02.1.01/0.0/0.0/16_019/0000760. The single crystal growth was supported in SUSU by the Russian Foundation for Basic Research, RFBR (grant 20-08-00716). Additionally, DAV thanks the system of President's grants for young doctors of science (MD-5612.2021.4) for putting facilities at the author's disposal.

Author contributions

Alyabyeva L.N.: conceptualization, methodology, validation, formal analysis, investigation, data curation, writing – the original draft, visualization, project administration; Prokhorov A.S.: validation, formal analysis, writing - review & editing; Vinnik D.A.: – resources, investigation; Anzin V.B.: software, resources; Ahmed A.G.: investigation; Mikheykin A.: formal analysis; Bednyakov P.: investigation; Kadlec C.: investigation; Kadlec F.: resources, investigation, writing - review & editing; de Prado E.: formal analysis; Prokleška J.: resources; Proschek P.: investigation; Kamba S.: resources, writing - review & editing; Pronin A.V.: resources; Dressel M.: resources, writing - review & editing; Abalmasov V.A.: formal analysis; Dremov V.V.: resources, investigation; Schmid S.: investigation; Savinov M.: resources, investigation; Lunkenheimer P.: resources, formal analysis, investigation, writing – the original draft;

Gorshunov B.P.: conceptualization, validation, formal analysis, resources, writing - review & editing, supervision

Competing Interests statement

The authors declare no competing interests.

References

1. Sakai, K. & Tani, M. Introduction to Terahertz Pulses. in *Terahertz Optoelectronics* 1–30 (Springer-Verlag, 2005). doi:10.1007/10828028_1
2. Aghasi, H. *et al.* Terahertz electronics: Application of wave propagation and nonlinear processes. *Appl. Phys. Rev.* **7**, 021302 (2020).
3. Romanczyk, B. *et al.* W-Band Power Performance of SiN-Passivated N-Polar GaN Deep Recess HEMTs. *IEEE Electron Device Lett.* **41**, 349–352 (2020).
4. Song, H.-J. & Nagatsuma, T. Present and Future of Terahertz Communications. *IEEE Trans. Terahertz Sci. Technol.* **1**, 256–263 (2011).
5. Tonouchi, M. Cutting-edge terahertz technology. *Nat. Photonics* **1**, 97–105 (2007).
6. Williams, B. S. Terahertz quantum-cascade lasers. *Nat. Photonics* **1**, 517–525 (2007).
7. Wang, P. S. & Xiang, H. J. Room-Temperature Ferrimagnet with Frustrated Antiferroelectricity: Promising Candidate Toward Multiple-State Memory. *Phys. Rev. X* **4**, 011035 (2014).
8. Kimura, T. Magnetolectric Hexaferrites. *Annu. Rev. Condens. Matter Phys.* **3**, 93–110 (2012).
9. Laguta, V. *et al.* Magnetolectric coupling in multiferroic Z-type hexaferrite revealed by electric-field-modulated magnetic resonance studies. *J. Mater. Sci.* **55**, 7624–7633 (2020).

10. Zhai, K. *et al.* Giant magnetoelectric effects achieved by tuning spin cone symmetry in Y-type hexaferrites. *Nat. Commun.* (2017). doi:10.1038/s41467-017-00637-x
11. Chun, S. H. *et al.* Electric Field Control of Nonvolatile Four-State Magnetization at Room Temperature. *Phys. Rev. Lett.* **108**, 177201 (2012).
12. Shen, S.-P. *et al.* Quantum electric-dipole liquid on a triangular lattice. *Nat. Commun.* **7**, 10569 (2016).
13. Shen, S.-P. *et al.* Magnetic-ion-induced displacive electric polarization in FeO₅ bipyramidal units of (Ba,Sr)Fe₁₂O₁₉ hexaferrites. *Phys. Rev. B* **90**, 180404 (2014).
14. Harris, V. G. Modern Microwave Ferrites. *IEEE Trans. Magn.* **48**, 1075–1104 (2012).
15. Zuo, X., How, H., Somu, S. & Vittoria, C. Self-Biased Circulator/Isolator at Millimeter Wavelengths Using Magnetically Oriented Polycrystalline Strontium M-Type Hexaferrite. in *IEEE Transactions on Magnetics* (2003). doi:10.1109/TMAG.2003.816043
16. Song, Y.-Y. Y., Sun, Y., Lu, L., Bevivino, J. & Wu, M. Self-biased planar millimeter wave notch filters based on magnetostatic wave excitation in barium hexagonal ferrite thin films. *Appl. Phys. Lett.* **97**, 173502 (2010).
17. Harris, V. G. *et al.* Recent advances in processing and applications of microwave ferrites. *J. Magn. Magn. Mater.* (2009). doi:10.1016/j.jmmm.2009.01.004
18. Pullar, R. C. Hexagonal ferrites: A review of the synthesis, properties and applications of hexaferrite ceramics. *Prog. Mater. Sci.* **57**, 1191–1334 (2012).
19. Gorbachev, E. A. *et al.* Hexaferrite materials displaying ultra-high coercivity and sub-terahertz ferromagnetic resonance frequencies. *Mater. Today* **32**, 13–18 (2020).
20. Gudkov, V. V. *et al.* Sub-lattice of Jahn-Teller centers in hexaferrite crystal. *Sci. Rep.* **10**, 7076 (2020).

21. Mikheykin, A. S. *et al.* Lattice anharmonicity and polar soft mode in ferrimagnetic M-type hexaferrite BaFe₁₂O₁₉ single crystal. *Eur. Phys. J. B* **87**, 232 (2014).
22. Zhukova, E. S. *et al.* Crucial influence of crystal site disorder on dynamical spectral response in artificial magnetoplumbites. *Solid State Sci.* **62**, 13–21 (2016).
23. Alyabyeva, L. N. *et al.* Influence of chemical substitution on broadband dielectric response of barium-lead M-type hexaferrite. *New J. Phys.* **21**, 063016 (2019).
24. Gorshunov, B. *et al.* Terahertz BWO-spectroscopy. *Int. J. Infrared Millimeter Waves* **26**, 1217–1240 (2005).
25. Ahmed, A. *et al.* Effect of aluminium substitution on low energy electrostatics of barium-lead M-type hexagonal ferrites. *J. Phys. Conf. Ser.* **1389**, 012044 (2019).
26. Alyabyeva, L. *et al.* Bi-relaxor behavior and Fe²⁺ fine structure in single crystalline Ba_{0.3}Pb_{0.7}Fe₁₂O₁₉M-type hexaferrite. in *2018 43rd International Conference on Infrared, Millimeter, and Terahertz Waves (IRMMW-THz)* 1–2 (IEEE, 2018).
doi:10.1109/IRMMW-THz.2018.8510000
27. Alyabyeva, L. *et al.* Terahertz-infrared electrostatics of lead-doped single crystalline Ba_{1-x}Pb_xFe₁₂O₁₉ M-type hexagonal ferrite. in *Proceedings of the 43rd International Conference on Infrared, Millimeter, and Terahertz Waves, IRMMW-THz* 1–2 (2018).
doi:10.1109/IRMMW-THz.2018.8510258
28. Lunkenheimer, P. *et al.* Colossal dielectric constants in transition-metal oxides. *Eur. Phys. J. Spec. Top.* **180**, 61–89 (2009).
29. Pyatakov, A. P. *et al.* Magnetically switched electric polarity of domain walls in iron garnet films. *EPL (Europhysics Lett.)* **93**, 17001 (2011).
30. Popov, M. A., Zavislyak, I. V. & Srinivasan, G. Current tunable barium hexaferrite millimeter wave resonator. *Microw. Opt. Technol. Lett.* **60**, 458–462 (2018).

31. Bierlich, S., Gellersen, F., Jacob, A. & Töpfer, J. Low-temperature sintering and magnetic properties of Sc- and In-substituted M-type hexagonal barium ferrites for microwave applications. *Mater. Res. Bull.* **86**, 19–23 (2017).
32. Alyabyeva, L. *et al.* Terahertz-infrared spectroscopy of Ti⁴⁺-doped M-type barium hexaferrite. *J. Alloys Compd.* **820**, 153398 (2020).
33. Kadlec, F. *et al.* Electromagnon in the Z-type hexaferrite (Ba_xSr_{1-x})₃Co₂Fe₂₄O₄₁. *Phys. Rev. B* **94**, 024419 (2016).
34. Vít, J. *et al.* Electromagnon in the Y-type hexaferrite BaSrCoZnFe₁₁AlO₂₂. *Phys. Rev. B* **97**, 134406 (2018).
35. Lines, M. E., Glass, A. M. & Burns, G. Principles and Applications of Ferroelectrics and Related Materials. *Phys. Today* **31**, 56–58 (1978).
36. Kamba, S. Soft-mode spectroscopy of ferroelectrics and multiferroics: A review. *APL Mater.* **9**, 020704 (2021).
37. Obradors, X., Collomb, A., Pernet, M., Samaras, D. & Joubert, J. C. X-ray analysis of the structural and dynamic properties of BaFe₁₂O₁₉ hexagonal ferrite at room temperature. *J. Solid State Chem.* **56**, 171–181 (1985).
38. Nakajima, Y. & Naya, S. Orientational Phase Transition and Dynamic Susceptibility of Hindered-Rotating Dipolar System –A Librator-Rotator Model–. *J. Phys. Soc. Japan* **63**, 904–914 (1994).
39. Normand, B. G. A., Giddy, A. P., Dove, M. T. & Heine, V. Bifurcation behaviour in structural phase transitions with multi-well potentials. *J. Phys. Condens. Matter* **2**, 3737–3745 (1990).
40. Onodera, Y. Dynamical Response of Ferroelectrics in Terms of a Classical Anharmonic-Oscillator Model. *J. Phys. Soc. Japan* **73**, 1216–1221 (2004).

41. Gorshunov, B. P. *et al.* Incipient ferroelectricity of water molecules confined to nano-channels of beryl. *Nat. Commun.* **7**, 12842 (2016).
42. Silva Júnior, F. M. & Paschoal, C. W. A. Spin-phonon coupling in BaFe₁₂O₁₉ M-type hexaferrite. *J. Appl. Phys.* **116**, 244110 (2014).
43. Chen, X.-B. *et al.* Raman studies of spin-phonon coupling in hexagonal BaFe₁₂O₁₉. *J. Appl. Phys.* **114**, 013912 (2013).
44. Izadkhah, H., Zare, S., Somu, S. & Vittoria, C. Effects of cobalt substitutions on the magnetoelectric coupling of M-type hexaferrite films. *Appl. Phys. Lett.* **106**, 142905 (2015).
45. Ebnabbasi, K., Mohebbi, M. & Vittoria, C. Room temperature magnetoelectric effects in bulk poly-crystalline materials of M- and Z-type hexaferrites. *J. Appl. Phys.* **113**, 17C703 (2013).
46. Mohebbi, M., Ebnabbasi, K. & Vittoria, C. First observation of magnetoelectric effect in M-type hexaferrite thin films. *J. Appl. Phys.* **113**, 17C710 (2013).
47. Kumar, K. & Pandey, D. Quantum phase transitions in Ba(1-x)CaxFe₁₂O₁₉ (0 ≤ x ≤ 0.10). *Phys. Rev. B* **96**, 024102 (2017).
48. Rowley, S. E. *et al.* Uniaxial ferroelectric quantum criticality in multiferroic hexaferrites BaFe₁₂O₁₉ and SrFe₁₂O₁₉. *Sci. Rep.* **6**, 25724 (2016).
49. Rowley, S. E. *et al.* Ferroelectric quantum criticality. *Nat. Phys.* **10**, 367–372 (2014).
50. Khmel'nitskii, D. E. & Shneerson, V. L. Russian version. *Sov. Phys. Solid State* **13**, 687 (1971).
51. Khmel'nitskii, D. E. & Shneerson, V. L. Phase transitions of the displacement type in crystals at very low temperatures. *Sov. J. Exp. Theor. Phys.* **37**, 164 (1973).

52. Harris, V. G. *et al.* Ba-hexaferrite films for next generation microwave devices (invited). *J. Appl. Phys.* **99**, 08M911 (2006).
53. Antonio-Lopez, J. E., Castillo-Guzman, A., May-Arrijoja, D. A., Selvas-Aguilar, R. & LiKamWa, P. Tunable multimode-interference bandpass fiber filter. *Opt. Lett.* **35**, 324 (2010).
54. Uher, J. & Hoefler, W. J. R. W. J. R. Tunable microwave and millimeter-wave band-pass filters. *IEEE Trans. Microw. Theory Tech.* **39**, 643–653 (1991).
55. Tan, G. & Chen, X. Structure and multiferroic properties of barium hexaferrite ceramics. *J. Magn. Magn. Mater.* **327**, 87–90 (2013).
56. Trukhanov, A. V. *et al.* Multiferroic properties and structural features of M-type Al-substituted barium hexaferrites. *Phys. Solid State* **59**, 737–745 (2017).
57. Karpov, D. *et al.* Nanoscale topological defects and improper ferroelectric domains in multiferroic barium hexaferrite nanocrystals. *Phys. Rev. B* **100**, 054432 (2019).
58. M. Born and E. Wolf. *Principles of Optics*. (Cambridge: Cambridge University Press, 1999).
59. Böhmer, R., Maglione, M., Lunkenheimer, P. & Loidl, A. Radio-frequency dielectric measurements at temperatures from 10 to 450 K. *J. Appl. Phys.* **65**, 901–904 (1989).

Supplementary Information

1. SI1. Crystals growth and characterization

High-quality single crystals of lead substituted barium hexaferrite, $\text{Ba}_{1-x}\text{Pb}_x\text{Fe}_{12}\text{O}_{19}$ ($x = 0.1$ and 0.2) were grown using by the flux technique with a Pt rod and PbO flux. After the crystals were separated from the crystallized flux, they were shaped to crystal plates up to 8 mm in size; their composition and unit cell parameters were determined using Energy-dispersive X-ray spectroscopy and powder X-ray diffraction. The chemical composition and calculated chemical

formulas are presented in Table 1. The obtained powder X-ray diffraction patterns on the $\text{Ba}_{0.9}\text{Pb}_{0.1}\text{Fe}_{12}\text{O}_{19}$ and $\text{Ba}_{0.8}\text{Pb}_{0.2}\text{Fe}_{12}\text{O}_{19}$ samples together with the literature data from ¹ presented in Figure SII-1 confirm the single-phase character of the samples and their magnetoplumbite-type (or *M*-type hexaferrite) structure. The calculated cell parameters values are presented in Table 2. The doping-induced changes in the cell parameters for are in good agreement with the previously published data ².

Table 1. Chemical composition and chemical formulas of the studied barium-lead hexaferrite crystals.

Elemental content, at. %			Calculated chemical formula
Fe	Pb	Ba	
33.95	0.32	2.49	$\text{Ba}_{0.9}\text{Pb}_{0.1}\text{Fe}_{12}\text{O}_{19}$
33.63	0.58	2.21	$\text{Ba}_{0.8}\text{Pb}_{0.2}\text{Fe}_{12}\text{O}_{19}$

Table 2. Experimental and literature data on unit cell parameters of the *M*-type hexaferrite crystals.

Sample formula	a [Å]	c [Å]	V [Å ³]	Ref.
$\text{BaFe}_{12}\text{O}_{19}$	5.893	23.194	697.5	³
$\text{BaFe}_{12}\text{O}_{19}$	5.8928(3)	23.201(3)	698.74	¹
$\text{Ba}_{0.9}\text{Pb}_{0.1}\text{Fe}_{12}\text{O}_{19}$	5.8936(3)	23.1753(16)	697.14(5)	Current work
$\text{Ba}_{0.8}\text{Pb}_{0.2}\text{Fe}_{12}\text{O}_{19}$	5.8948(3)	23.1780(8)	697.51(4)	Current work
$\text{PbFe}_{12}\text{O}_{19}$	5.873	23.007	687.24	⁴

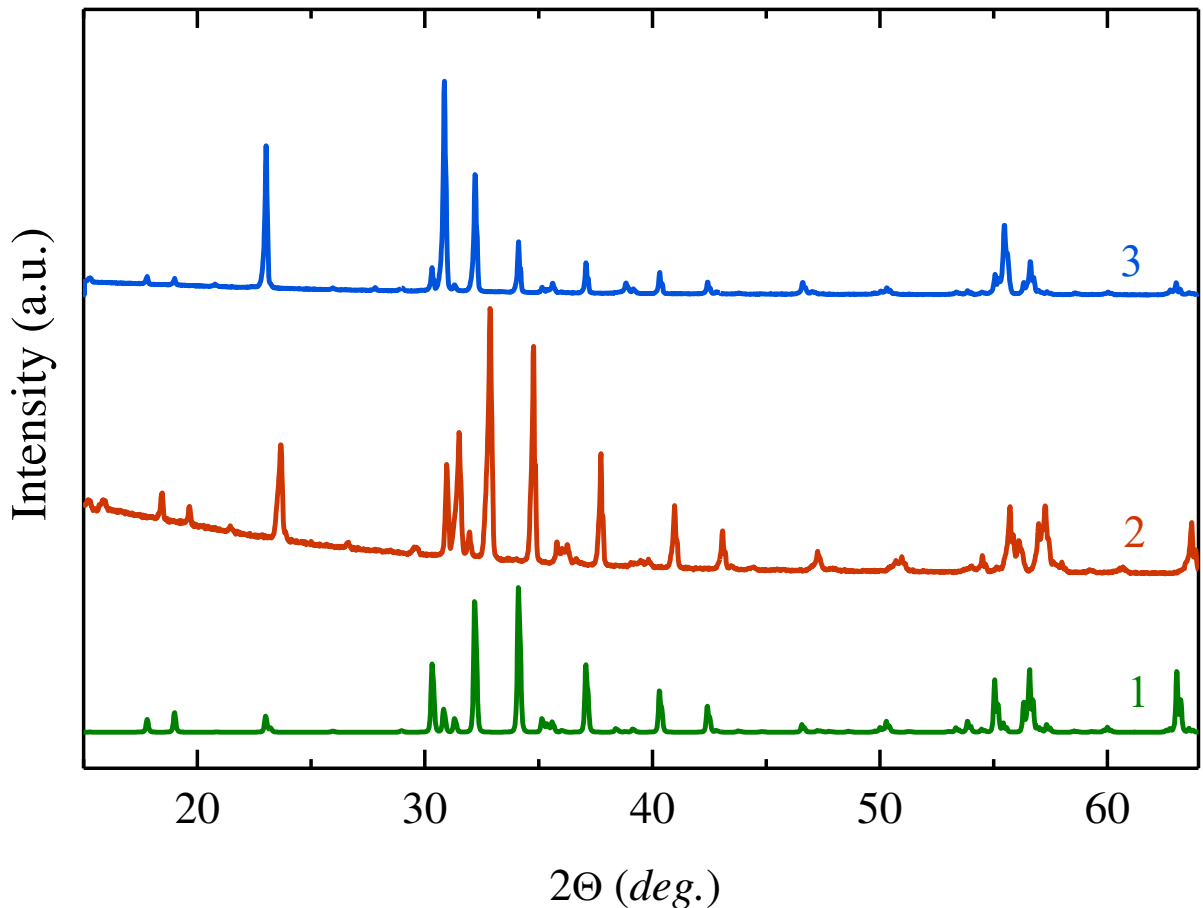


Figure SII-1. Powder XRD patterns of studied $\text{Ba}_{0.9}\text{Pb}_{0.1}\text{Fe}_{12}\text{O}_{19}$ (2) and $\text{Ba}_{0.8}\text{Pb}_{0.2}\text{Fe}_{12}\text{O}_{19}$ (1) together with literature data on pristine $\text{BaFe}_{12}\text{O}_{19}$ from ¹ (3). The patterns for different compounds are vertically shifted for reader's convenience.

The orientation of the crystals prepared for optical measurements was checked using XRD mapping; the samples were shown to be well oriented with a tilting of the c -axis from the surface normal no larger than 1.29 deg.

XRD measurements for the verification of the orientation were performed using Co radiation in a Panalytical X'Pert PRO diffractometer with a parallel-beam geometry, with the beam generated by a parabolic graded multilayer mirror (Göbel mirror). In order to ensure the parallelism in the diffracted beam, a parallel-plate collimator was employed. The diffractometer has a built-in Eulerian cradle which allows for measuring different crystallographic planes by turning the sample. The notation used below is shown in Figure SII-2.

Figure SII-2c represents the situation when the unit cells are not well oriented. It is necessary to turn the sample an angle (offset) in order to set the correct orientation of the planes for the diffraction to be observed. This offset then yields the misorientation of the unit cells with respect to the surface of the sample. Figure SII-1d shows the notation used for the axes and movements

performed by the diffractometer. Here ϕ is the sample azimuthal axis, ω is an axis perpendicular to the diffraction plane, and χ is the axis perpendicular to both ϕ and ω . The accuracy of the measurements around those axes are 0.05° in ϕ , 0.005° in ω and 0.05° in χ . In order to observe diffraction, the crystallographic planes must satisfy the Bragg's law given by Equation S11-1 where d is the inter-plane distance, θ is the Bragg angle, n the diffraction order and λ the wavelength of the radiation. For a non distorted hexagonal system, the inter-plane distance can be calculated by Equation S11-2 where h, k, l are the diffraction indices of the plane, and a, c denote the lattice parameters.

$$2d\sin\theta = n\lambda, \quad \text{Eq.S11 - 1}$$

$$\frac{1}{d^2} = \frac{4}{3} \left(\frac{h^2 + k^2 + kl}{a^2} \right) + \frac{l^2}{c^2}. \quad \text{Eq.S11 - 2}$$

We have calculated the misorientation of the unit cells and its lattice parameters for the sample $\text{Ba}_{0.9}\text{Pb}_{0.1}\text{Fe}_{12}\text{O}_{19}$. For calculating the misorientation, we measured a χ/ω map for the diffraction 008 corresponding to (008) atomic planes. In such a map the angle 2θ was fixed. Then for several χ angles the intensity of the diffraction as a function of ω was acquired. For this diffraction $2\theta = 35.908^\circ$, which was found using the 01-086-5547 PDF4 card for $\text{BaFe}_{12}\text{O}_{19}$ as a reference.

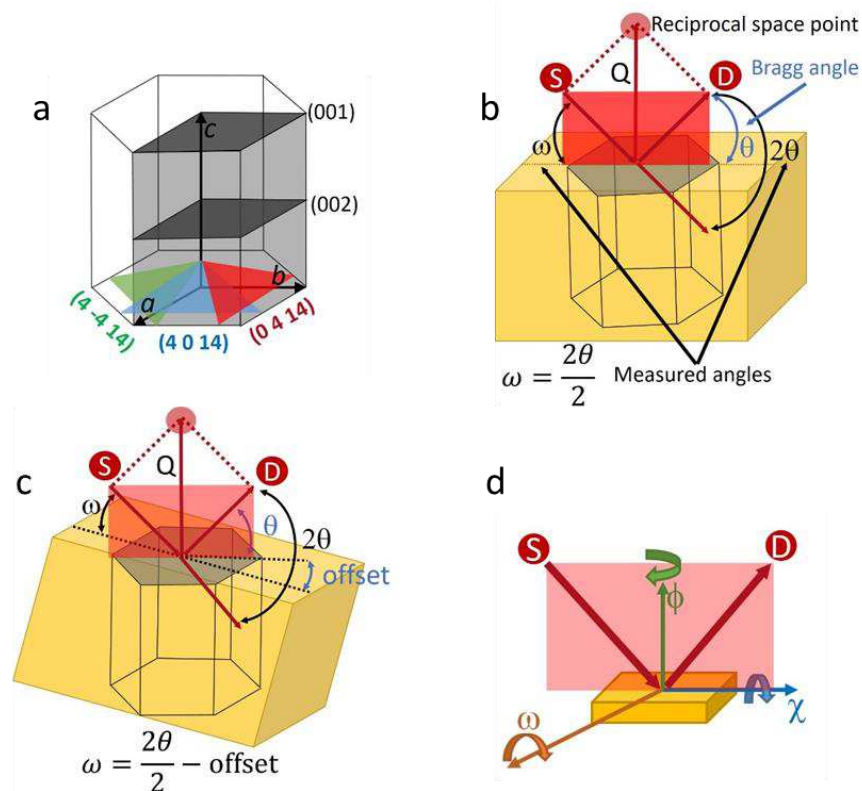


Figure SI1-2. (a) Hexagonal structure with the unit cell shaded. a , b and c are the lattice parameters; if the unit cell is not distorted, $a=b$. Several atomic c planes (001) and (002) are shown in dark gray. Three planes from the family $\{0\ 4\ 14\}$ are depicted in green, blue and red. (b) Sketch of a sample (in yellow) in which the unit cell is well oriented. The source (S), the detector (D), the diffraction vector (Q), the reciprocal space point and the diffraction plane are shown in red. ω is the angle between the incident beam and the surface of the sample, θ is the angle between the diffracted beam and the crystallographic plane, and 2θ is the angle between the incident and the diffracted beams. (c) Sketch of a not well oriented sample. The offset is the angle between the surface of the sample and the face of the unit cell. (d) Sketch of the turns and axes of the diffractometer. ϕ is the sample azimuthal axis, ω is an axis perpendicular to the diffraction plane and χ the axis perpendicular to both ϕ and ω .

The result is shown in Figure SI1-3, where the intensity of the peak is depicted on color contour lines as a function of χ and ω angles. The χ angle at which the intensity of the peak is maximal is marked by the horizontal black line. The horizontal dashed red line represents the angle at which the sample is not tilted around χ . The difference between these two lines corresponds to the misorientation around the χ axis.

As for the angle ω , the value at which the intensity is maximum is depicted by the vertical black line; the position at which the sample is not tilted around this axis ($\omega = \theta$) is outside of the range of the measurement. It is obvious that the situation illustrated in Figure SI1-2b is not satisfied since

$$19.248 = \omega \neq \frac{2\theta}{2} = 17.954 \rightarrow \text{offset} = 1.294 .$$

These measured tilts indicate that in order to orient the unit cell, it is necessary to tilt the sample by 0.56° around the χ axis and by 1.29° around the ω axis.

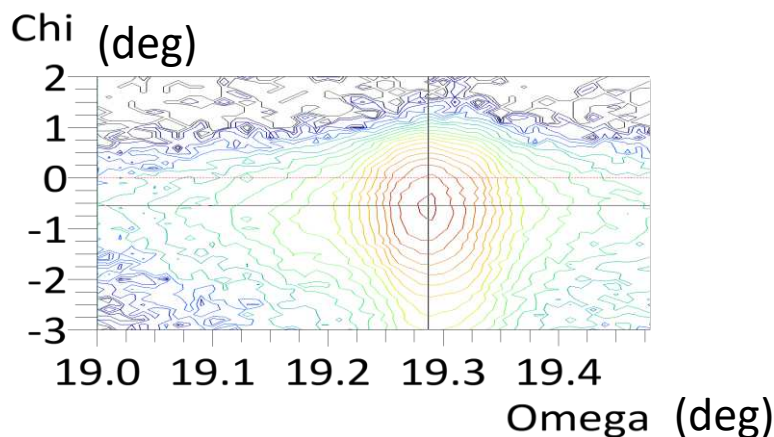


Figure SI1-3: χ/ω map for the 008 diffraction peak, showing the intensity by color contour lines as a function of χ and ω angles. The solid black lines denote the position of the peak intensity maximum. The horizontal dotted line in red indicates the position in which the sample is not tilted around the χ axis. The position in which the sample is not tilted around the ω axis is outside the range of the measurement.

A reciprocal space map (RSM) consists of a two-dimensional dependence of the intensity distribution around a given point in the reciprocal space (around the diffraction peak in the angular space) as a function of its coordinates q_x and q_y . The relations between the angles 2θ and ω in the angular space and the coordinates q_x and q_y in the reciprocal space are shown in Figure SI1-4.

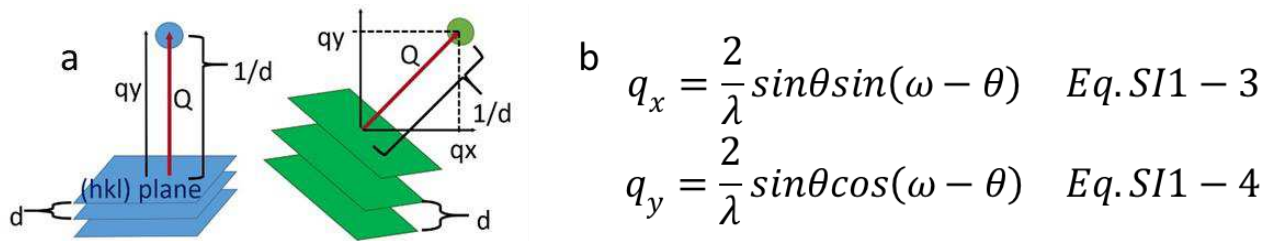


Figure SI1-4. (a) Sketch of the reciprocal space coordinates for two different set of planes and (b) equations relating the measurements in the angular and reciprocal spaces.

In order to find out whether the lattice is distorted, several measurements belonging to the same family of planes and performed at different ϕ angles must be done. The multiplicity of the planes $\{0\ 4\ 14\}$ is 12 but only 6 of their corresponding diffraction peaks are accessible to the measurement. We have calculated the lattice parameters through RSMs from the diffraction peaks 0 0 8, 0 0 20, and 6 maps (three of them are shown in FigureSI1-2a) from the family of planes $\{0414\}$. Two of those maps are presented in Figure SI1-5.

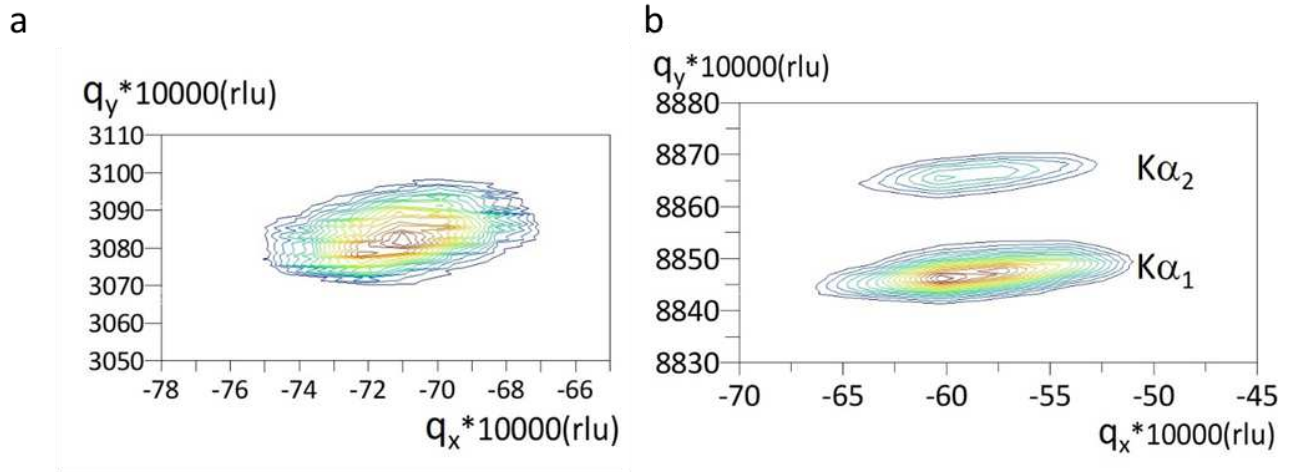


Figure SII-5. RSMs for the diffraction peak (a) 008 and (b) 4 0 14. In (b), the bottom and top peaks belong to $K\alpha_1$ and $K\alpha_2$ spectral lines from the Co anode, respectively. rlu (reciprocal-lattice unit) = $2/\lambda \text{ \AA}^{-1}$.

Using Eqs. SII-1 – SII-4, we obtained the lattice parameters values as follows:

$a=5.893 \text{ \AA}$, $b=5.894 \text{ \AA}$, and $c= 23.201 \text{ \AA}$ with an estimated uncertainty of $\pm 0.005 \text{ \AA}$.

Since, within the estimated error, $a=b$, we can conclude that the distortion amounts to $\varepsilon = (0.0\% \pm 0.1\%)$.

SI2. Structure and Infrared polar phonons

A convenient description of the magnetoplumbite structure relies on the concept of layered modules stacked along the hexagonal c axis. This concept is applied to a wide range of long-period hexagonal ferrites of natural and artificial origins⁵⁻⁷. In the case of M -type hexaferrites, the modules are formed by two fundamental types of blocks: the S – block with the formula $[B_6O_8]^{2+}$ and the R-block with the formula $[AB_6O_{11}]^{2-}$ where $A=\text{Ba, Sr, Pb}$ and $B=\text{Fe}$. The S block has the structure of cubic spinel. The R layer consists of two kinds of columns, one being the trigonal bipyramidal element, and the other consisting of two stacked octahedral units. These columns are connected through equatorial edges of bipyramids and edges of shared facets. A framework of columns forms a set of cuboctahedral voids occupied by the divalent ions. Figure SI2-1 shows a segment of the magnetoplumbite type crystal structure built of the two basic blocks, R and S. These two blocks form the so-called M-block. The next in the sequence is the M block again that is turned by 180 degrees around the c axis. The asterisks in Figure SI2-1 indicate this block rotation. This stacking of two M-blocks rotated by 180 degrees relative to each other forms the unit cell of magnetoplumbite crystal structure.

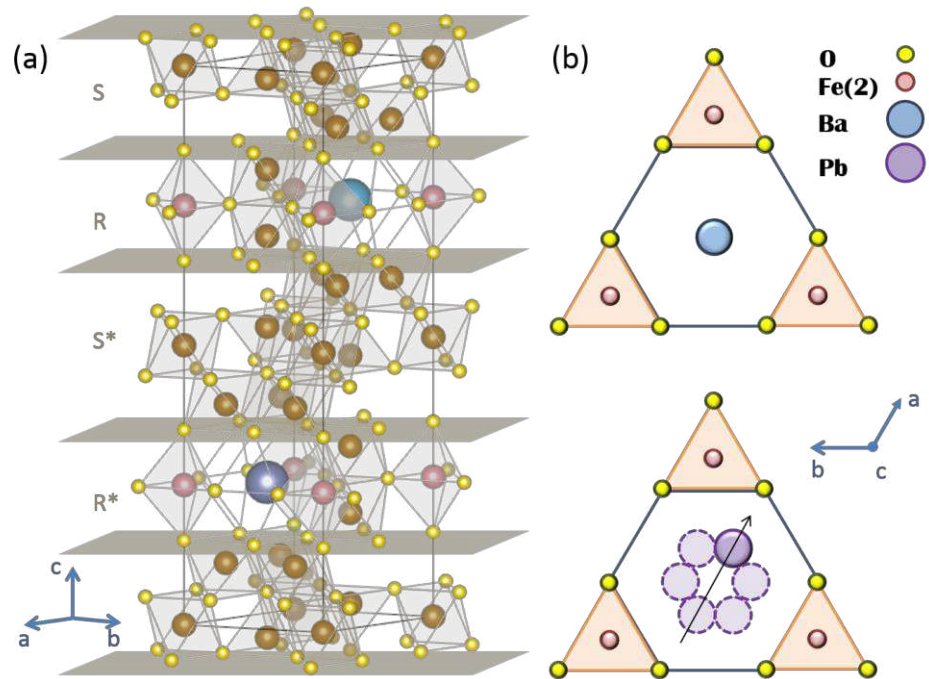


Figure SI2-1. Panel (a): stack of fundamental blocks that form the crystal structure of the M-type hexaferrite. The S and R blocks boundaries are indicated by yellow planes. The black lines indicate the unit cell of the crystal structure. Big balls correspond to large A^{2+} ions (for the compositions studied in this work, $A^{2+} = \text{Ba}$ or Pb), middle-size balls indicate Fe ions (pink ones are iron ions, located in 2b positions, that surround the A^{2+} cuboctahedra), small bright-yellow balls are oxygen ions. Panel (b): schematic illustration of appearance of a dipole moment in the ab -plane. The Ba ion is located in the center of the polyhedron with all Ba-O bonds of equal length (top), while Pb is shifted towards one of the oxygen vertices (bottom), thus inducing a dipole moment (black arrow). The Pb ion can hop among six potential minima, which can be considered as a reorientation of the dipole moment around the c -axis.

Figure SI2-2 demonstrates room-temperature THz-IR spectra of reflection coefficient of $\text{Ba}_{1-x}\text{Pb}_x\text{Fe}_{12}\text{O}_{19}$ samples with $x=0.1$ and $x=0.2$ measured for polarization $E \perp c$. In the THz range the reflectivity was calculated from the complex dielectric permittivity spectra using the Fresnel expressions. The spectra above 1000 cm^{-1} are smooth and contain few information; we used the flat phonon tails of reflectivity primarily to obtain the high-frequency values of dielectric permittivity. A set of excitations seen in the region $90\text{-}1000 \text{ cm}^{-1}$ are associated with polar lattice vibrations. Out of 17 E_{1u} phonon modes, predicted by the factor-group analysis (ref. [19] from the main text), we detected 14 lines for both compositions.

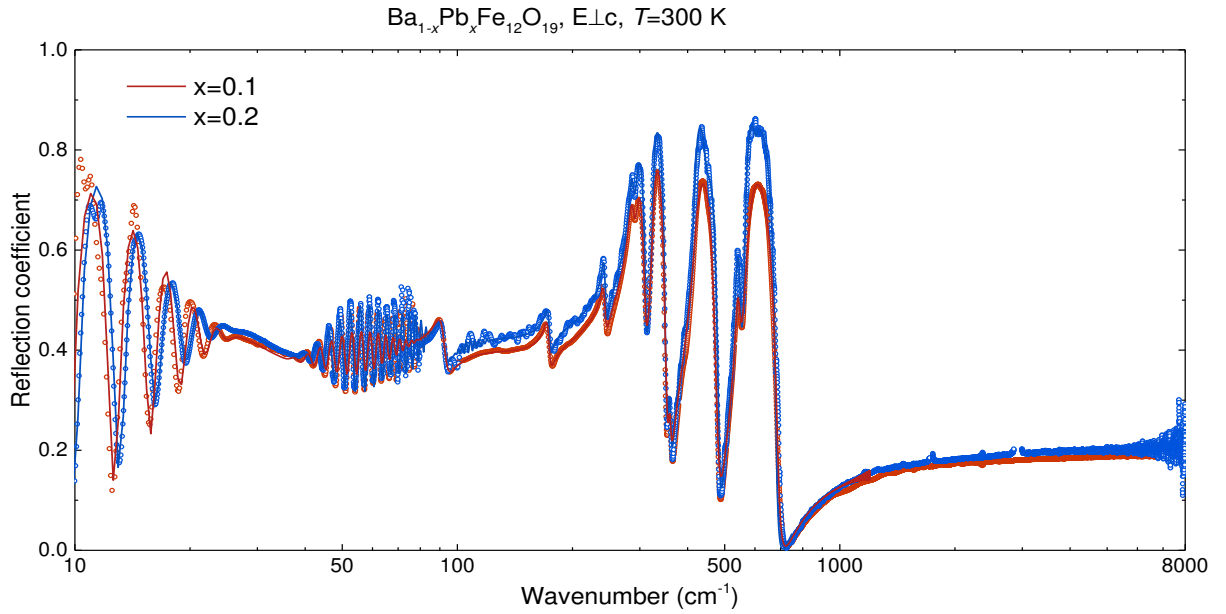


Figure SI2-2. Room-temperature spectra of reflection coefficient of $\text{Ba}_{1-x}\text{Pb}_x\text{Fe}_{12}\text{O}_{19}$ with $x=0.1$ (red) and $x=0.2$ (blue) measured for polarization $E \perp c$. Open dots are experimental data; solid lines correspond to modeling using Equation (1) to calculate the reflectivity spectra as described in the text. Spectra below $\approx 100 \text{ cm}^{-1}$ correspond to measured infrared data and to the reflectivity calculated from complex THz dielectric permittivity. Oscillations in the spectra below $\approx 20 \text{ cm}^{-1}$ and between 40 and 80 cm^{-1} are due to interference of the radiation within the plane-parallel sample (Fabry-Perot effect).

SI3. Relaxations in radio frequency range

Havriliak-Negami parameters of dielectric relaxation spectra of $\text{Ba}_{1-x}\text{Pb}_x\text{Fe}_{12}\text{O}_{19}$ crystals are provided in Figure SI3-1.

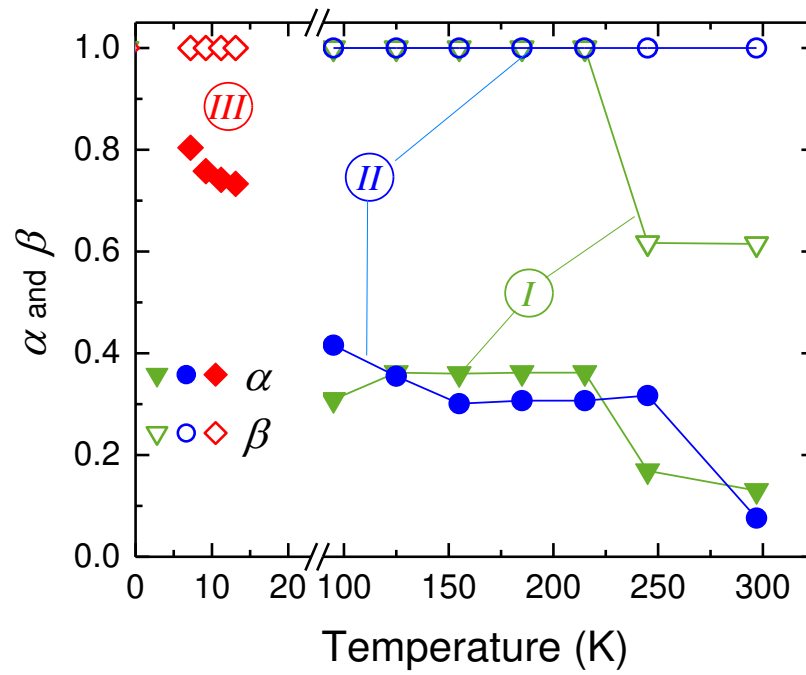


Figure SI3-1. Temperature dependences of parameters α (solid symbols) and β (open symbols) obtained by least-square fitting of radio-frequency dielectric spectra of real and imaginary parts of dielectric permittivity (Figure 2) with the Havriliak-Negami expression (Eq. 2 in the main text). The Roman numerals in circles denote the three relaxational processes visible in the spectra (Figure 2 in the main text).

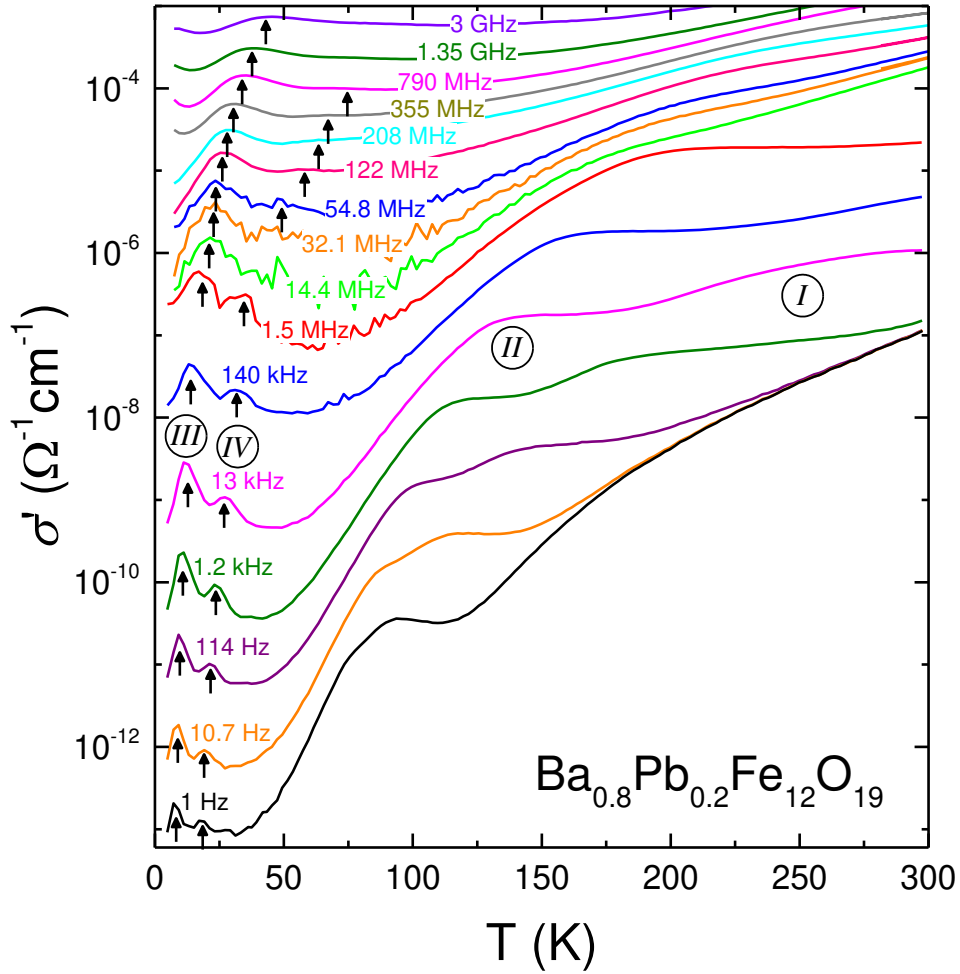


Figure SI3-2. Temperature dependence of the real part of the AC conductivity of $\text{Ba}_{1-x}\text{Pb}_x\text{Fe}_{12}\text{O}_{19}$ with $x = 0.2$, measured for polarization $E \perp c$. Results are shown for various frequencies between 1 Hz and 3 GHz. At frequencies above 100 MHz, the absolute values are of low precision (uncertainty of about a factor of two), whereas the relative temperature variation is of high significance, allowing for a meaningful estimate of the peak temperatures. Arrows indicate the positions of the two intrinsic low-temperature relaxation peaks used for estimates of their temperature-dependent relaxation times, shown by open symbols in Figure 3b. For the 13 kHz curve, the numbering of the four detected relaxational processes (non-intrinsic: I and II; intrinsic: III and IV) is indicated. The Roman numerals in circles denote the four relaxational processes visible in the spectra (Figs. 2 and 3 in main text).

SI4. Heat capacity of $\text{Ba}_{1-x}\text{Pb}_x\text{Fe}_{12}\text{O}_{19}$, $x=0.1$

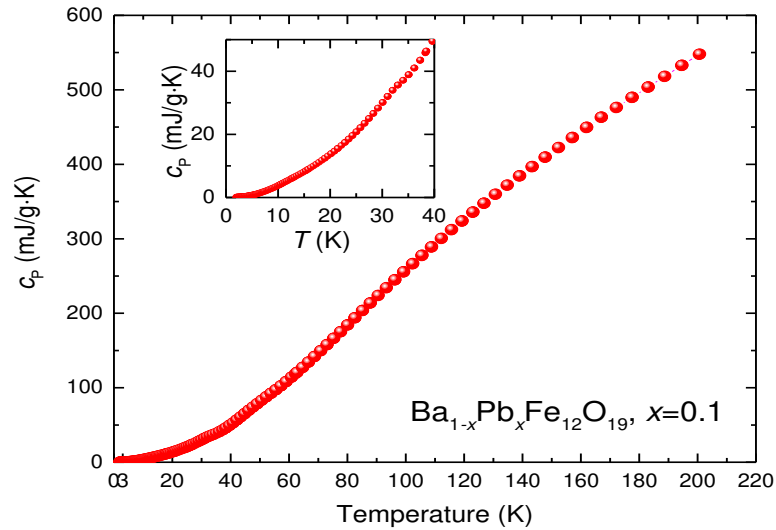


Figure SI4-1. Temperature dependence of heat capacity of the $\text{Ba}_{1-x}\text{Pb}_x\text{Fe}_{12}\text{O}_{19}$, $x=0.1$, single crystal. Inset shows $c_p(T)$ behavior at low temperatures.

SI5. Magnetic/electric Force Microscopy

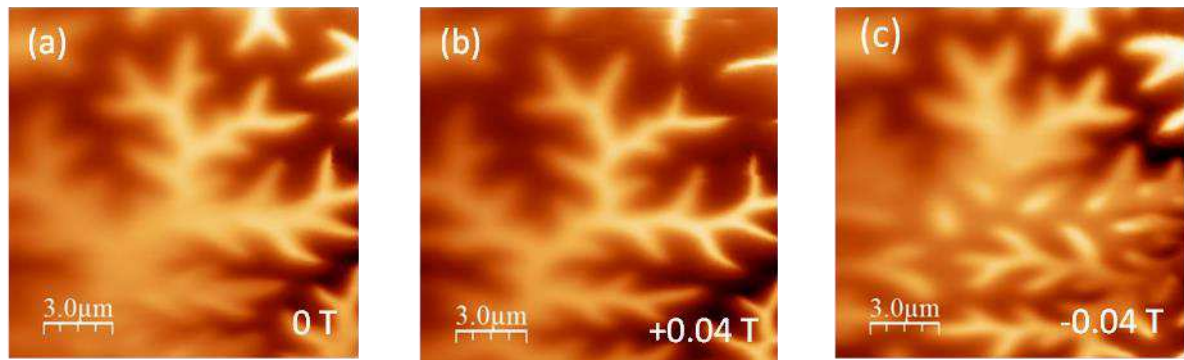
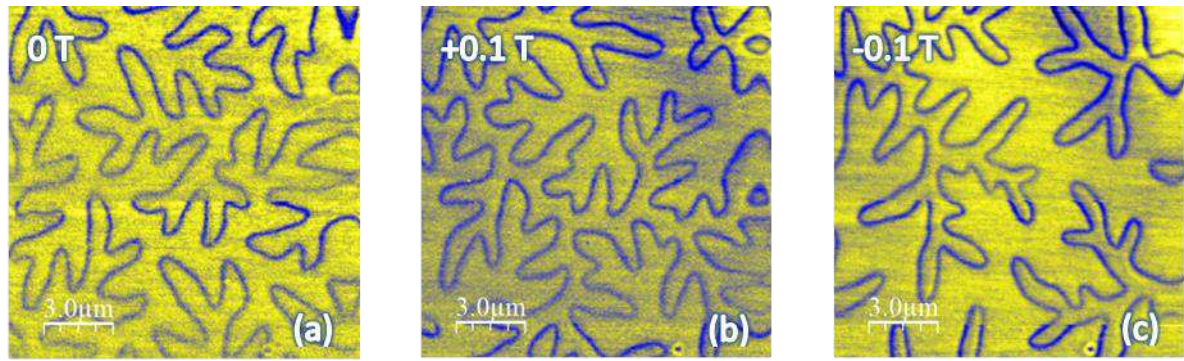
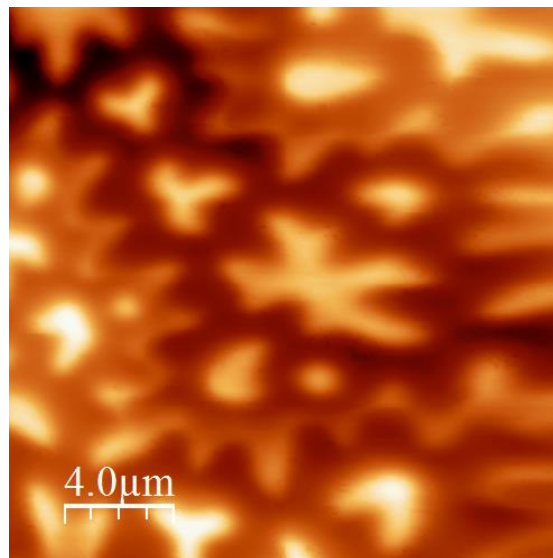


Figure SI5-1. MFM images of $\text{BaFe}_{12}\text{O}_{19}$ single crystal obtained at $T=5$ K under external magnetic field of 0 T (a), +0.04 T (b) and -0.04 T (c). In the mode of constant distance (lift=150nm) between the tip and the sample cleaved surface, the shift of the cantilever frequency under PLL control was measured. The observed change in contrast across the scanned field is associated with the unavoidable slope of the sample surface. Changes in the shapes of the domains caused by the external field are clearly visible. The crystallographic c -axis is perpendicular to the sample surface.



FigureSI5-2. EFM images of $\text{BaFe}_{12}\text{O}_{19}$ single crystal at $T=5$ K. The image was obtained by measuring the shift in resonance frequency of a nonmagnetic cantilever covered with PtIr film, in the mode of constant distance (lift=50 nm) between the tip and the cleaved sample surface. At the magnetic domains walls, there is an electric field gradient causing the resonance frequency shift. The observed domain walls change their positions and shapes depending on the applied external magnetic field of 0 T (a), 0.1 T (b) and -0.1 T (c). A defect visible at the bottom of the images can serve as a reference point for comparison. The crystallographic c -axis is perpendicular to the sample surface.



FigureSI5-3. MFM image of a $\text{Ba}_{1-x}\text{Pb}_x\text{Fe}_{12}\text{O}_{19}$ single crystal ($x=0.2$) at $T=5$ K in zero magnetic field. The emanated magnetic field repolarizes the MFM tip⁸. The phase map was obtained with a lift of 150 nm. The crystallographic c -axis is perpendicular to the sample surface.

SI6. Magnetic relaxation in the radio-frequency spectra of $\text{Ba}_{1-x}\text{Pb}_x\text{Fe}_{12}\text{O}_{19}$, $x=0.1$

In the spectra of complex magnetic susceptibility of single crystalline $\text{Ba}_{0.9}\text{Pb}_{0.1}\text{Fe}_{12}\text{O}_{19}$, at frequencies from 0.1 Hz to 1490 Hz, we detected a relaxational process; its characteristic frequency shifts with temperature, see FigureSI6-1. We note that this relaxation occurs within the same frequency region as the dielectric relaxations I and II observed in the spectra of

dielectric permittivity, below 1 MHz, see Figure 2 in the main text. Both relaxations red-shift during cooling. We connect both relaxations with the domains dynamics similar to those observed in the compound with a higher concentration of lead, $\text{Ba}_{0.3}\text{Pb}_{0.7}\text{Fe}_{12}\text{O}_{19}$ ⁹. The temperature-activated behavior of the corresponding relaxation time is presented in FigureSI6-2.

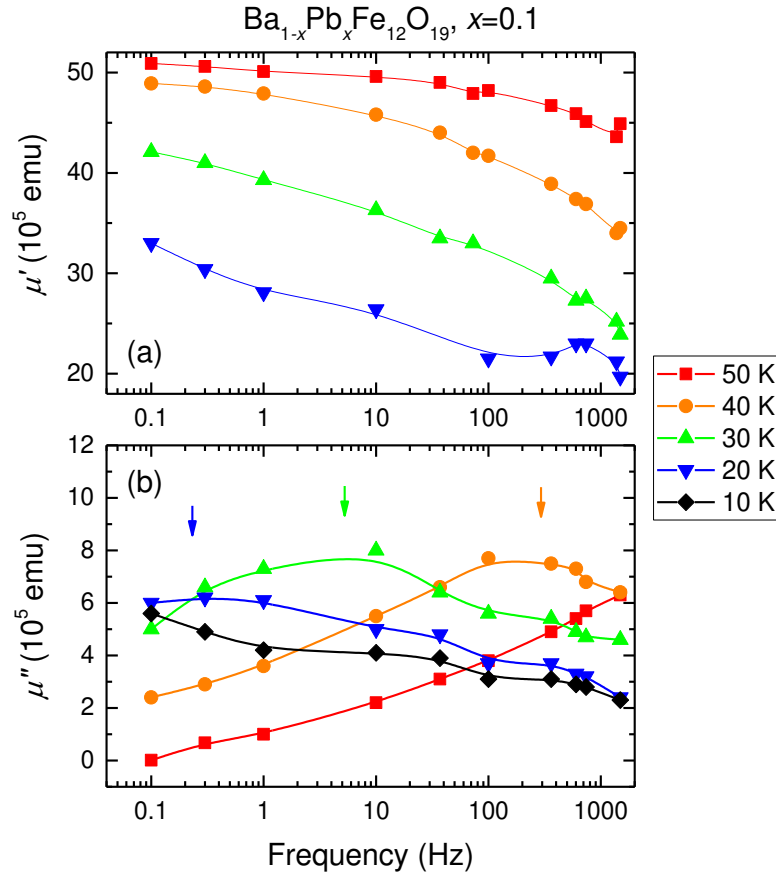


Figure SI6-1. Spectra of real μ' (a) and imaginary μ'' (b) parts of complex magnetic susceptibility $\mu^* = \mu' + i\mu''$ of $\text{Ba}_{1-x}\text{Pb}_x\text{Fe}_{12}\text{O}_{19}$, $x=0.1$, crystal measured at different temperatures for driving magnetic field $H_{ac} \parallel c$. The magnetic resonance enters the useful frequency window at a temperature between 40 and 50 K, and it moves outside the window at about 10 K. Arrows indicate the positions of the magnetic absorption peaks.

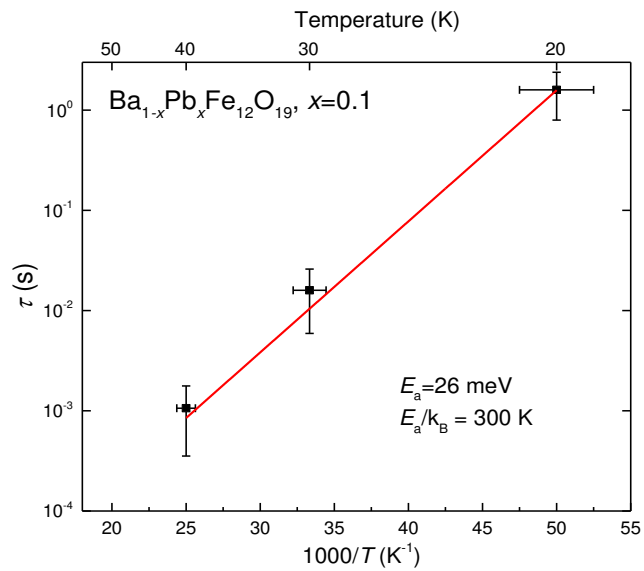


Figure SI16-2. Arrhenius plot of the magnetic relaxation time characteristic of the relaxational band observed in spectra of magnetic susceptibility for the $\text{Ba}_{1-x}\text{Pb}_x\text{Fe}_{12}\text{O}_{19}$, $x=0.1$, crystal for driving magnetic field $H_{ac} \parallel c$ (Figure SI6-1). Line shows activated behavior.

SI7. Gigahertz peak in the spectra of $\text{Ba}_{1-x}\text{Pb}_x\text{Fe}_{12}\text{O}_{19}$, $x=0.2$

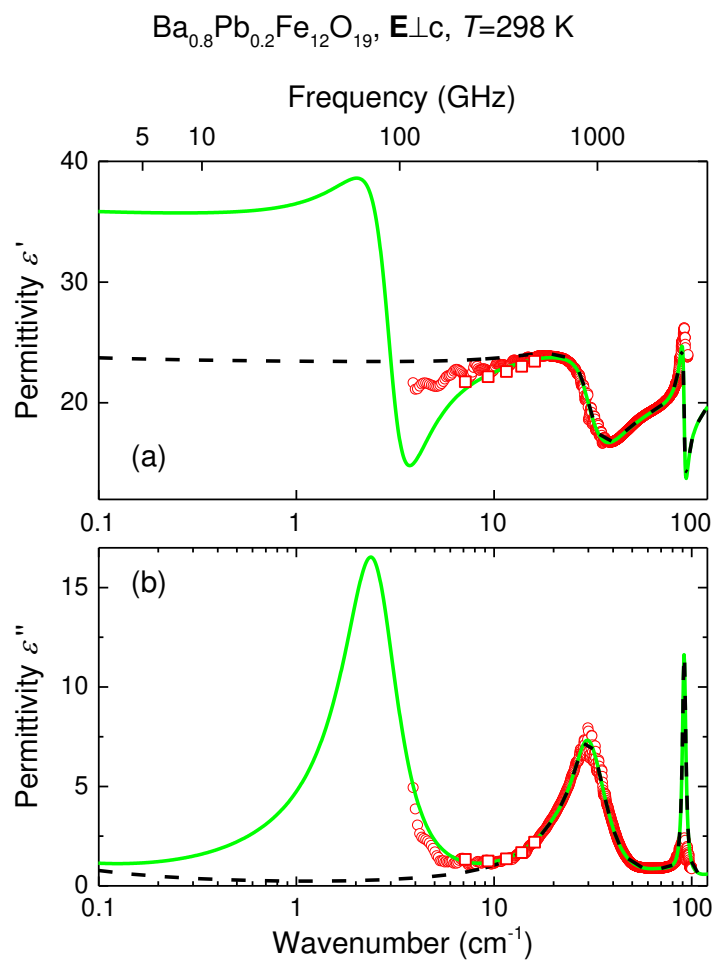


Figure SI7-1. Room temperature THz spectra of real (a) and imaginary (b) parts of complex dielectric permittivity of $\text{Ba}_{1-x}\text{Pb}_x\text{Fe}_{12}\text{O}_{19}$, $x=0.2$, for polarization $E \perp c$. Open squares represent the data obtained at frequencies of interference maxima in the transmission coefficient of the plane-parallel sample; this data provides an enhanced accuracy in the determination of dielectric parameters¹⁰. Full green lines show the results of a least-square fit that takes into account the dispersion in the experimental spectra below 20 cm^{-1} and yields a radio-frequency real permittivity of $\epsilon' \approx 30-35$ (Figure 1 in main text); the fit evidences an excitation at $\approx 2 \text{ cm}^{-1}$. Dashed black lines correspond to a model without the spectral dispersion below 20 cm^{-1} , yielding a wrong value of the radio-frequency permittivity.

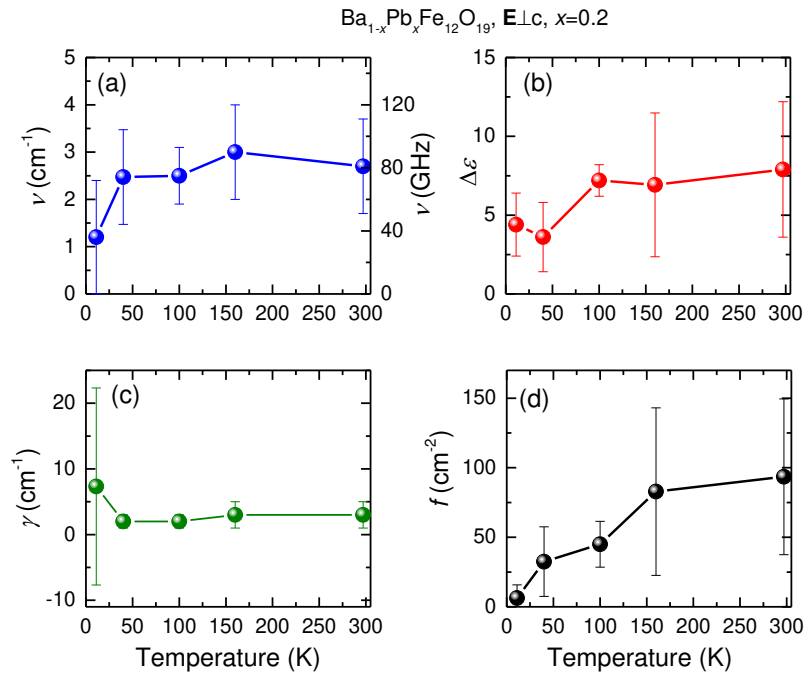


Figure SI7-2. Temperature dependences of parameters of the absorption peak detected near $\approx 2 \text{ cm}^{-1}$ (Figure SI7-1) in the spectra of $\text{Ba}_{1-x}\text{Pb}_x\text{Fe}_{12}\text{O}_{19}$, $x=0.2$, for polarization $E \perp c$: resonance frequency (a), dielectric strength (b), damping constant (c) and oscillator strength (d).

SI8. Ferromagnetic resonance in $\text{Ba}_{1-x}\text{Pb}_x\text{Fe}_{12}\text{O}_{19}$, $x=0.1$

We measured the reflectivity spectra in the frequency range where the THz soft mode is located ($20-60 \text{ cm}^{-1}$), and the complex transmissivity at lower frequencies ($4-30 \text{ cm}^{-1}$), under varying external magnetic fields (EMF) $\mu_0 H_{\text{EMF}}=0-7 \text{ T}$ where μ_0 is the vacuum permeability. In the transmissivity spectra we detected a shallow resonance that enters the measurement frequency window at $H_{\text{EMF}}=3 \text{ T}$ and shifts to higher frequencies with the increase of the EMF. The peak frequency of the resonance linearly depends on the field with the slope $k=0.95 \pm 0.5 \text{ cm}^{-1}/\text{T}$. The field-dependent frequency can be expressed as¹¹:

$$\omega g \frac{\mu_B}{\hbar} H_{EMF} \mu_0, \quad (\text{SI8-1})$$

where g is the g -factor. From the above expression for hexaferrite with $g=2$ ¹² we obtained $\nu[\text{cm}^{-1}] \sim 0.93 \mu_0 H_{EMF}(T)$ which is consistent with our observation (Figure SI8-1). Extrapolation of $\nu(H_{EMF})$ to $H_{EMF}=0$ gives the peak frequency of the FMR at zero field $\nu(H_{EMF}=0)=1.7 \pm 0.2 \text{ cm}^{-1}$ ($51 \pm 6 \text{ GHz}$), a value typical of hexaferrites¹³.

We can exclude the coupling between the THz soft excitation and the observed ferromagnetic resonance which would lead to a transfer of the soft mode intensity, since the oscillator strength $\Delta\mu\nu^2$ of the resonance is temperature independent, Figure SI7-2(d).

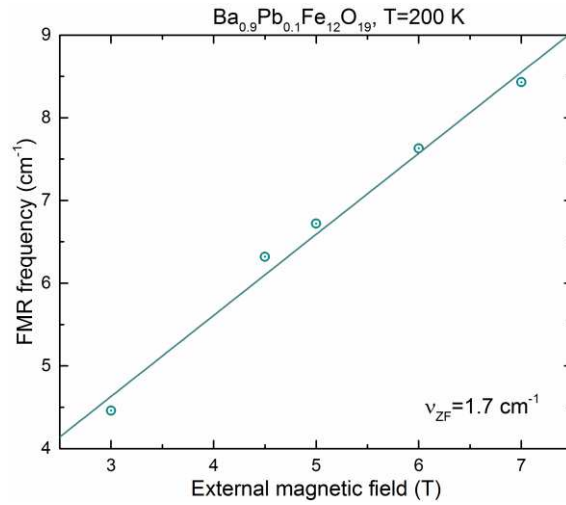


Figure SI8-1. Frequency position of the ferromagnetic resonance as a function of external magnetic field in $\text{Ba}_{1-x}\text{Pb}_x\text{Fe}_{12}\text{O}_{19}$ with $x = 0.1$ for polarization $E \perp c$. Dots are experimental data; line represents a linear approximation with Eq (SI8-1). Extrapolation of the model to the zero frequency gives the value of the FMR $\nu_{ZF}=1.7 \pm 0.2 \text{ cm}^{-1}$ or (51 ± 6) GHz.

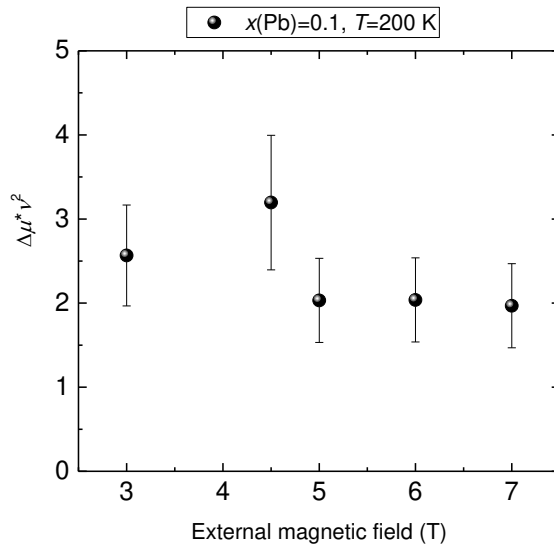


Figure SI8-2. Oscillator strength of the ferromagnetic resonance as a function of external magnetic field.

SI9. Dielectric origin of the THz soft mode in $\text{Ba}_{1-x}\text{Pb}_x\text{Fe}_{12}\text{O}_{19}$

The magnetic or dielectric origin of the soft absorption line seen in the THz spectra can be identified according to the spectral shape of reflection coefficient spectrum. Two basic models used to describe the resonances are dielectric and magnetic Lorentzian lineshapes given, respectively, by equations: for the dielectric one,

$$\varepsilon^* = \varepsilon' + i\varepsilon'' = \frac{\Delta\varepsilon_j v_j^2}{(v_j^2 - v^2) + i v \gamma_j} \quad (\text{SI9-1})$$

Here $f_j = \Delta\varepsilon_j v_j^2$ is the oscillator strength of the j -th resonance, $\Delta\varepsilon_j$ is its dielectric strength (dielectric contribution), v_j represents the resonance frequency, γ_j is the damping factor; and for the magnetic one,

$$\mu^* = \mu' + i\mu'' = \frac{\Delta\mu_j v_j^2}{(v_j^2 - v^2) + i v \gamma_j} \quad (\text{SI9-2})$$

Here μ' and μ'' are real and imaginary parts of complex magnetic susceptibility $\mu^* = \mu' + i\mu''$, $\Delta\mu_j v_j^2$ is the oscillator strength of the j -th resonance, $\Delta\mu_j$ is its magnetic strength (magnetic contribution), v_j represents the resonance frequency, and γ_j is the damping factor. With the above expressions, spectra of reflection $R(v)$ and transmission $Tr(v)$ coefficients of plane-parallel samples can be calculated using standard Fresnel expressions. It is known that unlike transmissivity, magnetic and dielectric resonances show up differently in the reflectivity $R(v)$ spectra¹⁴. This fact was used to determine the character of the THz soft mode seen in the terahertz spectra of $\text{Ba}_{1-x}\text{Pb}_x\text{Fe}_{12}\text{O}_{19}$ compounds. We modeled the room temperature transmissivity spectra of the soft mode for $x=0.2$ compound separately with dielectric and magnetic Lorentzians, Eqs. SI9-1, SI9-2, respectively. Having the obtained parameters, we reconstructed the reflection coefficient spectra for both cases. Utilizing the Fourier transform IR-spectrometer Bruker 113v equipped with a far-IR bolometer detector, we measured directly the reflection coefficient in the range 25-80 cm^{-1} . Three sets of data collected are shown in Figure SI9-1, clearly indicating a dielectric origin of the THz resonance.

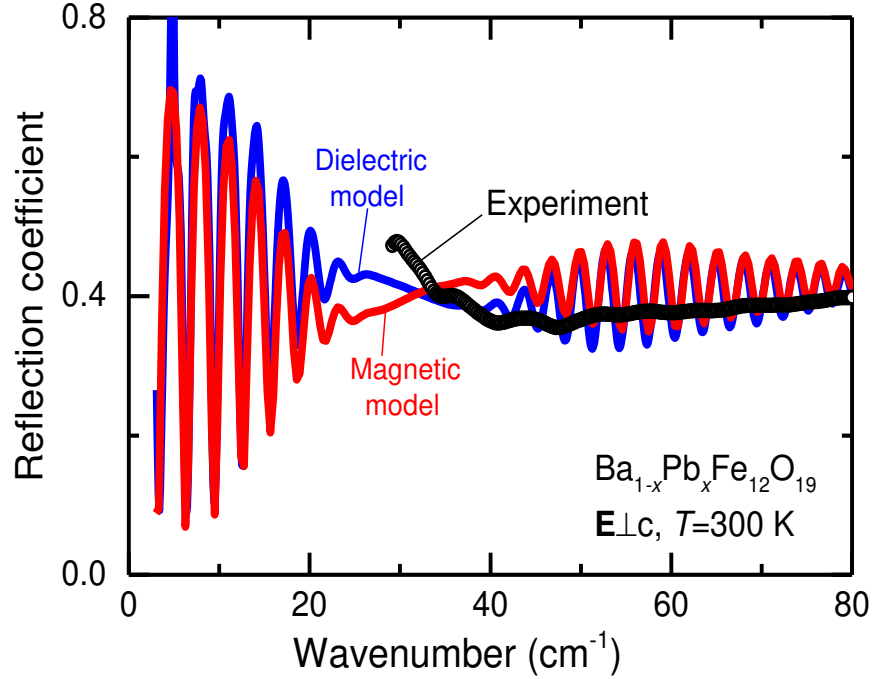


Figure SI9-1. Black dots show room-temperature spectrum of reflection coefficient of $\text{Ba}_{1-x}\text{Pb}_x\text{Fe}_{12}\text{O}_{19}$, $x=0.2$, crystal measured for polarization $E \perp c$. Solid lines correspond to results of least-square fitting of transmission coefficient spectrum, modeling the soft-mode resonance with a dielectric Lorentzian, Eq (SI9-1), (blue) and magnetic Lorentzian, Equation (SI9-2) (red).

SI10. Possible anharmonic mechanism of THz mode softening

The peculiar dependence of the THz soft mode on temperature, $\nu \propto (T - T_c)^\delta$ with $\delta \approx 0.25$, observed in our experiment can be explained by ion oscillations in the quartic potential of the form $V(Q) = (a/2)Q^2 + (b/4)Q^4$. Indeed, for large values of the coordinate Q , a thermal-averaged harmonic part of the potential $V(Q + \Delta Q)$ as a function of the fluctuation ΔQ can be written as $\langle V_h(\Delta Q) \rangle = (a + 3b\langle Q^2 \rangle) \Delta Q^2 / 2$. For small values of the coefficient, $a \approx 0$, which can be expected for small values of T_c , the thermal average of the coordinate in the classical limit (at high temperatures) is given by the equipartition theorem as $b\langle Q^4 \rangle = k_B T$. Thus, we can estimate $\langle Q^2 \rangle = (k_B T / 3b)^{1/2}$ (where we have assumed $\langle Q^4 \rangle = 3\langle Q^2 \rangle^2$ as for the normal distribution), and we get a temperature dependence of the soft-mode frequency, $\omega^2 \approx (3bk_B T)^{1/2} / m$, close to that observed experimentally.

According to recent X-ray diffraction data², only Pb and Fe(2) ions have large mean square displacements in the ab -plane, which may indicate an anharmonicity of their potentials: for $x = 0.23, 0.44, \text{ and } 0.8$, the square displacements are $0.0252, 0.0436 \text{ and } 0.0687 \text{ \AA}^2$ for the Ba/Pb ions and $0.0097, 0.0114 \text{ and } 0.0155 \text{ \AA}^2$ for the Fe(2) ions, respectively. We assume that the

largest displacements correspond to the Pb and Fe ions potentials whereas the smaller ones are due to the presence of Ba ions and statistical averaging. Given the measured phonon frequency of about $\omega = 2\pi \cdot 30 \text{ cm}^{-1}$ at $T = 300 \text{ K}$, we estimate $b = 8054 \text{ meV \AA}^{-4}$ for the Pb ions and $b = 584 \text{ meV \AA}^{-4}$ for the Fe(2) ions. The calculated ground state square displacement of 0.0219 \AA^2 for the Fe(2) ion in the potential with the above coefficient b and $a = 0$ is consistent with the experimental data. At the same time, the calculated square displacement for the Pb ion, 0.0059 \AA^2 , turns out to be significantly smaller. Thus, we conclude that the observed soft mode may be due to anharmonic softening of Fe(2) ion oscillations. These ions lie in the same plane as Ba/Pb ions, and they can be affected by the nearest Ba/Pb substitution.

With the energy spectrum E_n and wave functions of the Fe(2) ions in the quartic potential, we calculate the corresponding imaginary part of the dielectric susceptibility¹⁵

$$\alpha'' = \frac{1}{\hbar Z} \sum (e^{-E_n/k_B T} - e^{-E_m/k_B T}) \frac{|x_{nm}|^2 \gamma_{nm}}{(\nu + \nu_{nm})^2 + \gamma_{nm}^2}, \quad (\text{SI10-1})$$

where $Z = \sum e^{-E_n/k_B T}$ is the partition function, $\nu_{nm} = (E_n - E_m)/\hbar$ is the transition frequency between states n and m , x_{nm} is the matrix element of the coordinate along the electric field (which we suppose coincides with the coordinate Q) and γ_{nm} is the sum of the widths of two states. The calculated real part of the AC conductivity, $\sigma' = \nu \alpha''$, for $\gamma_{nm} = 10 \text{ cm}^{-1}$ is shown in Figure SI10-1 (this value characterizes electromagnetic absorption due to ionic oscillation).

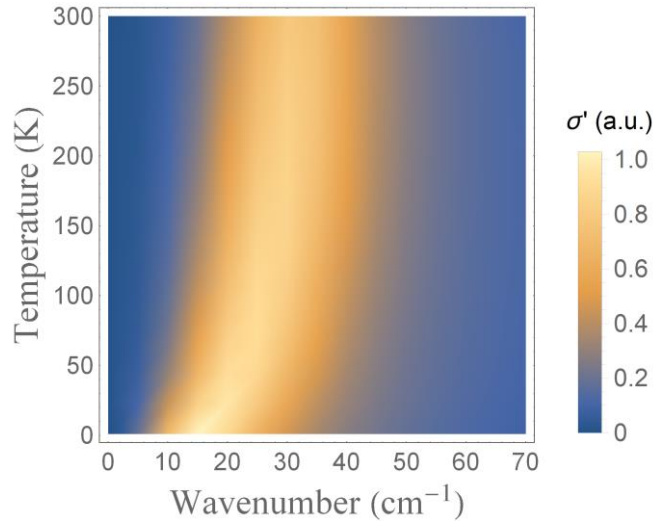


Figure SI10-1. Real part of the AC conductivity for Fe(2) ions in a quartic potential.

The frequency dependence of the calculated conductivity is close to that observed experimentally. However, the calculated conductivity value becomes larger at low temperatures, in contrast to our experiment. At the same time, our calculations are consistent with the available optical conductivity calculations in the quantum^{16–18} and classical^{19–22} approximations for an ion in the quartic potential. Note that a decrease in conductivity at low temperature would occur

if the expression SI10-1 were further multiplied by the frequency ν , which could indicate the involvement of a density of states characteristic of acoustic phonons that produce a so-called boson peak around 1 THz in disordered systems²³. Another possible explanation for the discrepancy is an interaction between large-amplitude oscillations of Fe(2) ions and the magnetic system not taken into account in the calculations.

References

1. Kwon, S. J. A suggestion on the standard x-ray powder diffraction pattern of barium ferrite. *Powder Diffr.* **7**, 212–214 (1992).
2. Vinnik, D. *et al.* Magnetic and Structural Properties of Barium Hexaferrite BaFe₁₂O₁₉ from Various Growth Techniques. *Materials (Basel)*. **10**, 578 (2017).
3. Townes, W. D., Fang, J. H. & Perrotta, A. J. The crystal structure and refinement of ferrimagnetic barium ferrite, BaFe₁₂O₁₉. *Zeitschrift für Krist.* **125**, 437–449 (1967).
4. Watanabe, K. Growth of minute barium ferrite single crystals from a Na₂O-B₂O₃ flux system. *J. Cryst. Growth* **169**, 509–518 (1996).
5. Pullar, R. C. Hexagonal ferrites: A review of the synthesis, properties and applications of hexaferrite ceramics. *Prog. Mater. Sci.* **57**, 1191–1334 (2012).
6. Delacotte, C. *et al.* Structure determination and crystal chemistry of large repeat mixed-layer hexaferrites. *IUCrJ* **5**, 681–698 (2018).
7. Kimura, T. Magnetolectric Hexaferrites. *Annu. Rev. Condens. Matter Phys.* **3**, 93–110 (2012).
8. Neu, V., Vock, S., Sturm, T. & Schultz, L. Epitaxial hard magnetic SmCo₅ MFM tips – a new approach to advanced magnetic force microscopy imaging. *Nanoscale* **10**, 16881–16886 (2018).
9. Alyabyeva, L. N. *et al.* Influence of chemical substitution on broadband dielectric response of barium-lead M-type hexaferrite. *New J. Phys.* **21**, 063016 (2019).
10. Gorshunov, B. *et al.* Terahertz BWO-spectroscopy. *Int. J. Infrared Millimeter Waves* **26**, 1217–1240 (2005).
11. Manuilov, S. A. & Grishin, A. M. Pulsed laser deposited films: Nature of magnetic anisotropy II Pulsed laser deposited Y₃Fe₅O₁₂ films: Nature of magnetic anisotropy II. *J. Appl. Phys. J. Appl. Phys. J. Appl. Phys. J. Appl. Phys. Appl. Phys. Lett.* (2010).
12. De Bitetto, D. J. Anisotropy Fields in Hexagonal Ferrimagnetic Oxides by Ferrimagnetic Resonance. *J. Appl. Phys.* **35**, 3482–3487 (1964).
13. Labeyrie, M., Mage, J., Simonet, W., Desvignes, J. & Le Gall, H. FMR linewidth of barium hexaferrite at millimeter wavelengths. *IEEE Trans. Magn.* **20**, 1224–1226 (1984).

14. Mukhin, A. A. *et al.* Submillimeter and far IR spectroscopy of magneto- and electro-dipolar rare-earth modes in the orthoferrite TmFeO₃. *Phys. Lett. A* **153**, 499–504 (1991).
15. Landau, L. D. & Lifshitz, E. M. *Course of theoretical physics. Vol. 5: Statistical physics. Statistical Physics* (1968).
16. Mashiyama, H., Eric Mkam Tchouobiap, S. & Ashida, M. Order–Disorder and Displacive Transitions in a Quantum Ising Model. *J. Phys. Soc. Japan* **77**, 084709 (2008).
17. Matsumoto, H. *et al.* Optical conductivity from local anharmonic phonons. *Phys. Rev. B* **79**, 214306 (2009).
18. Mori, T. *et al.* Optical conductivity of rattling phonons in type-I clathrate Ba₈G₁₆Ge₃₀. *Phys. Rev. B* **79**, 212301 (2009).
19. Onodera, Y. Dynamical Response of Ferroelectrics in Terms of a Classical Anharmonic-Oscillator Model. *J. Phys. Soc. Japan* **73**, 1216–1221 (2004).
20. Nakajima, Y. & Naya, S. Orientational Phase Transition and Dynamic Susceptibility of Hindered-Rotating Dipolar System –A Librator-Rotator Model–. *J. Phys. Soc. Japan* **63**, 904–914 (1994).
21. Onodera, Y. Dynamic Susceptibility of Classical Anharmonic Oscillator. *Prog. Theor. Phys.* **44**, 1477–1499 (1970).
22. Gorshunov, B. P. *et al.* Incipient ferroelectricity of water molecules confined to nano-channels of beryl. *Nat. Commun.* **7**, 12842 (2016).
23. Mori, T. *et al.* Optical Conductivity Spectral Anomalies in the Off-Center Rattling System β -Ba₈Ga₁₆Sn₃₀. *Phys. Rev. Lett.* **106**, 015501 (2011).

Figures

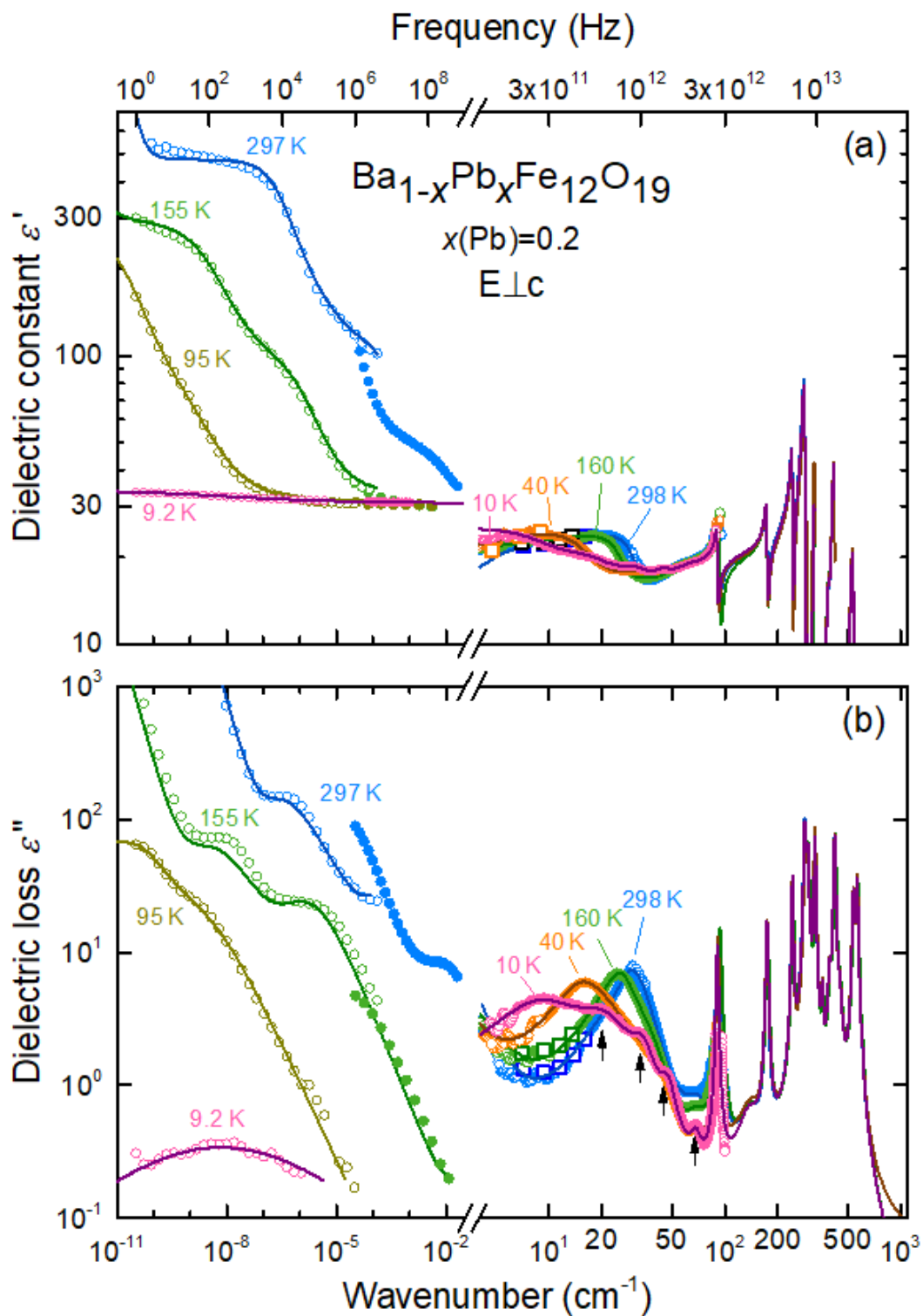


Figure 1

Broad-band (RF-THz-IR) spectra of real (a) and imaginary (b) parts of complex dielectric permittivity of $\text{Ba}_{1-x}\text{Pb}_x\text{Fe}_{12}\text{O}_{19}$, $x=0.2$... please see manuscript .pdf for full caption.

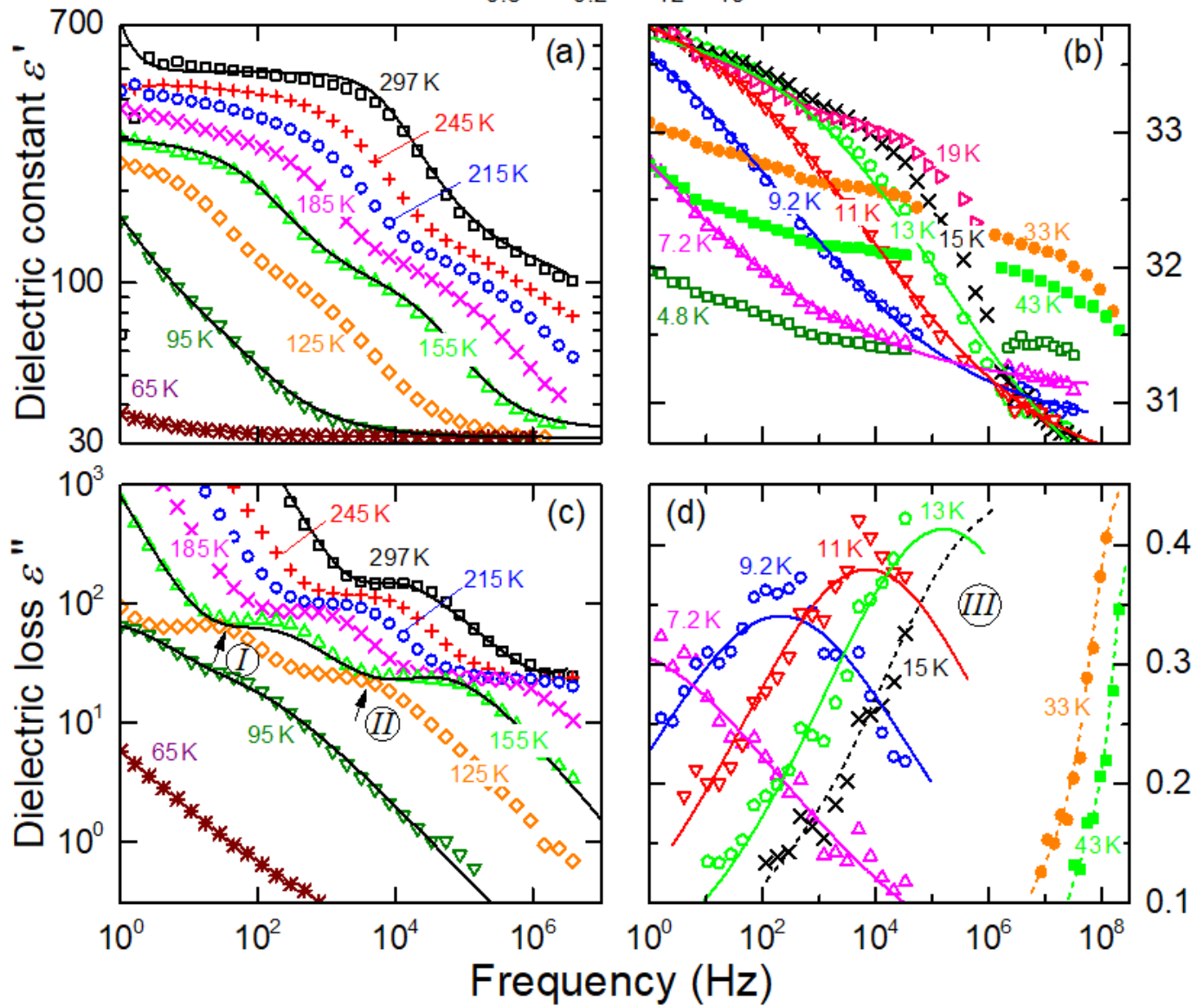
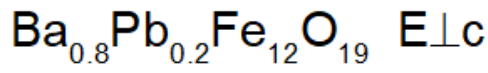


Figure 2

Radiofrequency spectra of the real (a,b) and imaginary (c,d) parts of the dielectric permittivity of $\text{Ba}_{1-x}\text{Pb}_x\text{Fe}_{12}\text{O}_{19}$, $x=0.2$... please see manuscript .pdf for full caption.

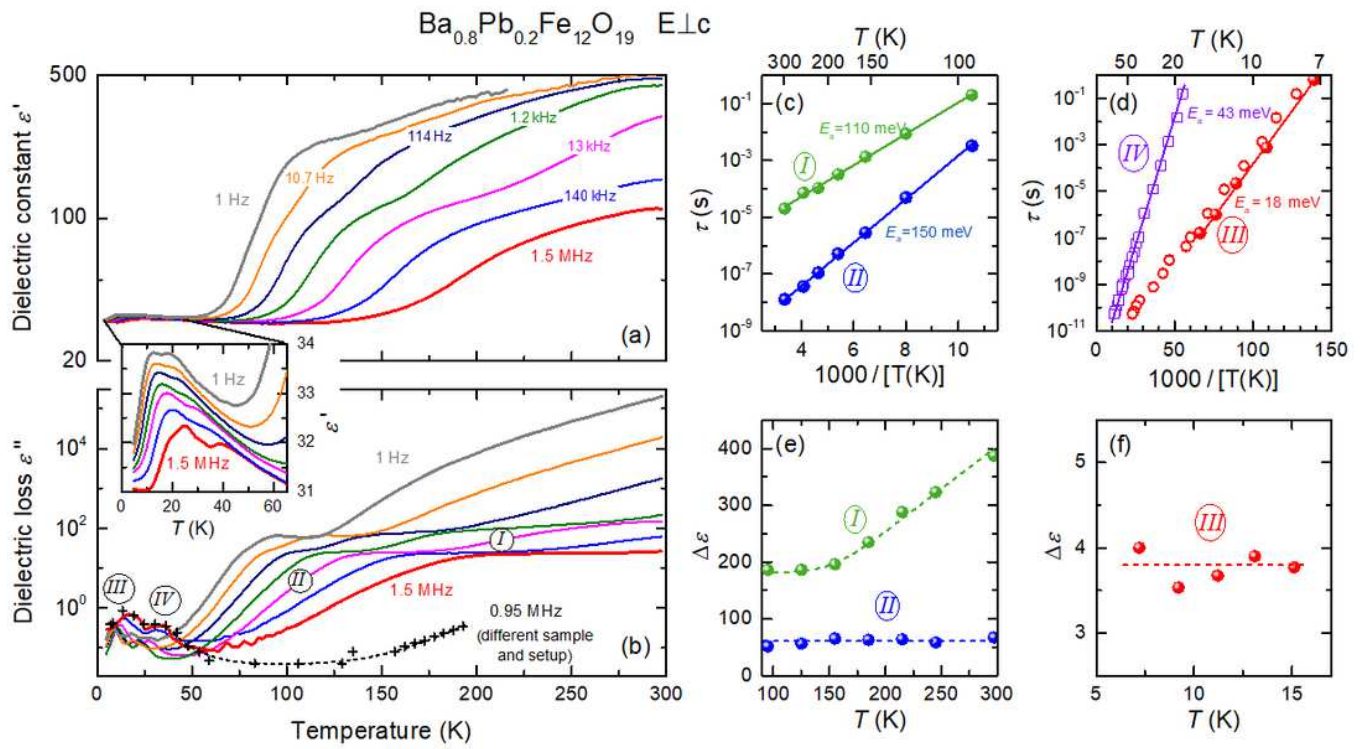


Figure 3

Temperature dependences of the real (a) and imaginary (b) parts of the dielectric permittivity of $\text{Ba}_{1-x}\text{Pb}_x\text{Fe}_{12}\text{O}_{19}$, $x=0.2$... please see manuscript .pdf for full caption.

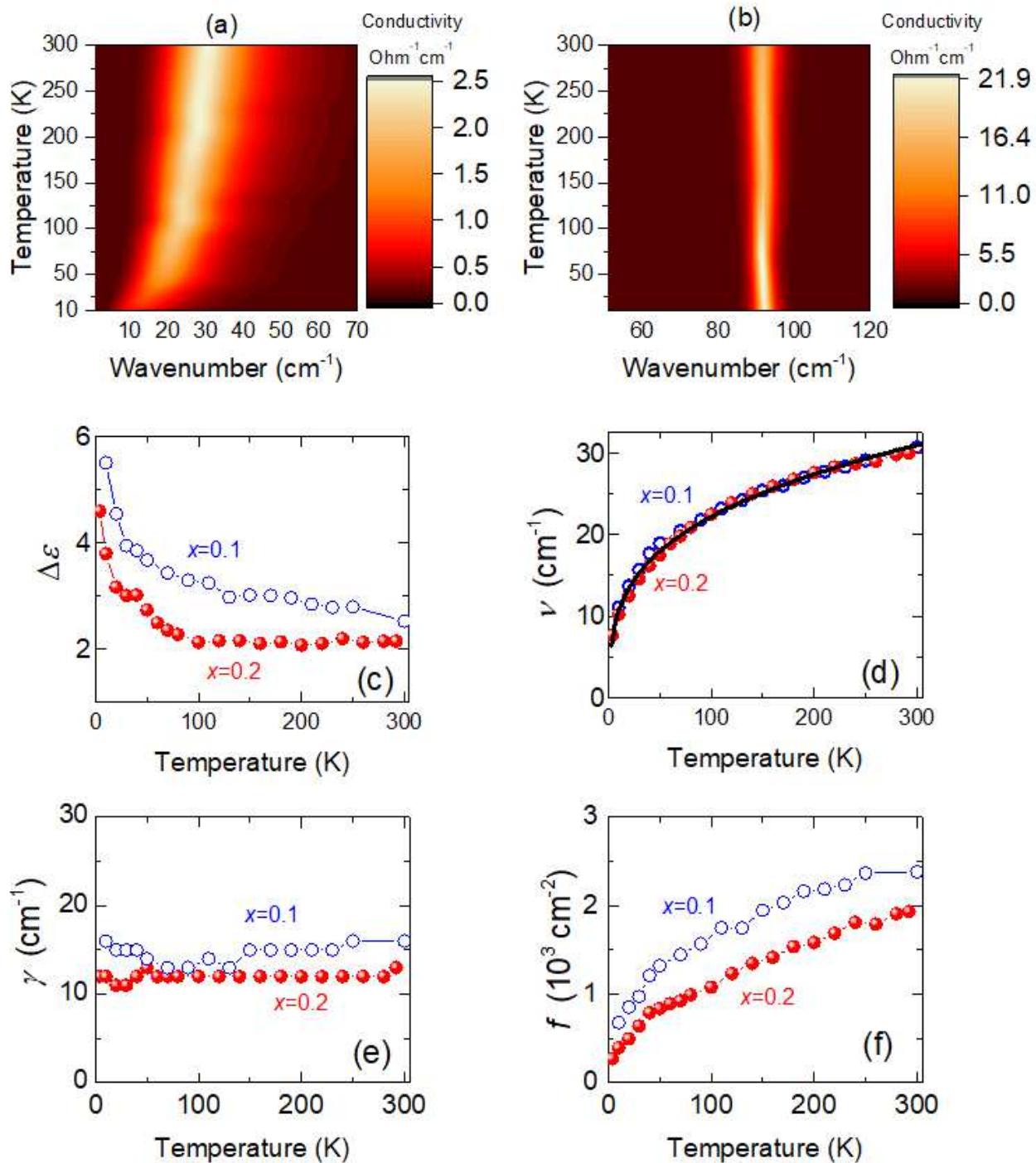
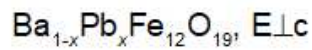


Figure 4

2D plots of temperature-dependent spectra of the real part of AC conductivity of the THz soft excitation (a) and the lowest E1u optical phonon (b) for the $\text{Ba}_{1-x}\text{Pb}_x\text{Fe}_{12}\text{O}_{19}$ crystal, $x=0.1$. Panels (c-f): parameters of the soft THz excitation as a function of temperature for $\text{Ba}_{1-x}\text{Pb}_x\text{Fe}_{12}\text{O}_{19}$, $x=0.1$ and $x=0.2$ crystals: dielectric strength (c), resonance frequency (d), damping factor (e) and oscillator strength (f). Please see manuscript .pdf for full caption.